The Role of Trp Side Chains in Tuning Single Proton Conduction through Gramicidin Channels

Joseph A. Gowen,* Jeffrey C. Markham,* Sara E. Morrison,* Timothy A. Cross,† David D. Busath,* Eric J. Mapes,‡ and Mark F. Schumaker‡

*Zoology Department and Center for Neuroscience, Brigham Young University, Provo, Utah 84602; †Center for Interdisciplinary Magnetic Resonance at the National High Field Laboratory, Institute of Molecular Biophysics and Department of Chemistry, Florida State University, Tallahassee, Florida 32306; and ‡Department of Mathematics, Washington State University, Pullman, Washington 99164 USA

ABSTRACT We present an extensive set of measurements of proton conduction through gramicidin A (gA), B (gB), and M (gM) homodimer channels which have 4, 3, or 0 Trp residues at each end of the channel, respectively. In gA we find a shoulder separating two domains of conductance increasing with concentration, confirming the results of Eisenman, G., B. Enos, J. Hagglund, and J. Sandblom. 1980. *Ann. NY. Acad. Sci.* 339:8–20. In gB, the shoulder is shifted by ~½ pH unit to higher H^+ concentrations and is very sharply defined. No shoulder appears in the gM data, but an associated transition from sublinear to superlinear *I-V* values occurs at a 100-fold higher $[H^+]$ in gM than in gA. The data in the low concentration domain are analyzed using a configuration space model of single-proton conduction, assuming that the difference in the proton potential of mean force (PMF) between gA and its analogs is constant, similar to the results of Anderson, D., R. B. Shirts, T. A. Cross, and D. D. Busath. 2001. *Biophys. J.* 81:1255–1264. Our results suggest that the average amplitudes of the calculated proton PMFs are nearly correct, but that the water reorientation barrier calculated for gA by molecular dynamics using the PM6 water model (Pomès, R., and B. Roux. 1997. *Biophys. J.* 72:246*a*) must be reduced in amplitude by 1.5 kcal/mol or more, and is not rate-limiting for gA.

INTRODUCTION

The gramicidin A (gA) monomer is a pentadecapeptide consisting of alternating L and D amino acids. The conducting form of the channel is an N-terminal to N-terminal dimer composed of two identical $\beta^{6.5}$ helices. The channel is 25 Å long, with a central pore diameter of 4 Å (Arsenyev et al., 1990; Ketchem et al., 1997). The amino acid side chains extend radially outward, away from the helical backbone. These include four pairs of tryptophans at positions 9, 11, 13, and 15 positioned near the lipid-water interface. The tryptophan indole ring system has a dipole moment of ~2.1 Debye (Cotten et al., 1999b), comparable to that of a water molecule (Duca and Jordan, 1998). The orientations and dynamics of the indoles in the membrane and their dipole moment have been studied by solid-state NMR (Hu et al., 1993, 1995; Hu and Cross, 1995; Cotten et al., 1999b) and molecular modeling (Woolf and Roux, 1997; Dorigo et al., 1999; Anderson et al., 2001). The indole dipole moments contribute substantially to the electrical potential in the pore region. There is reasonable agreement (Hu and Cross, 1995) between the approximate magnitude of the dipole potential from the atomistic force field computations (Woolf and Roux, 1997; Dorigo et al., 1999; Anderson et al., 2001) and the effects of Trp-to-Phe changes on the Na^+ conductance measured experimentally (Becker et al., 1991). However, the shape of the axial potential profile from the Trp side chains depends on the force field used. The results of Anderson et al. (2001), based upon an ab initio force field, are particularly simple. They find that the indoles of each tryptophan pair stabilize cations in the pore by ~0.6 kcal/mol. This change is approximately constant throughout the channel, independent of the spatial coordinate parallel to the pore axis, and presumably is extinguished by bulk electrolyte shielding just outside the channel.

An extensive set of gramicidin analogs have been developed and investigated by Andersen, Busath, Cukierman, Cross, Heitz, Koeppe, Woolley, and others (e.g., Andersen et al., 1998; Busath et al., 1998; Cotten et al., 1999b; Quigley et al., 2000; Jaikaran and Woolley, 1995; for reviews of earlier work, see Woolley and Wallace, 1992; Busath, 1993). In gramicidin B (gB), the tryptophans at position 11 are replaced by phenylalanine. The indole residues of the tryptophans are located outside the beta helix ~7 or 8 Å from the pore axis (Cotten et al., 1999b). The phenylalanine side chain is not expected to have a significant dipole moment. Therefore, it appears likely that differences between the conductance properties of gB and gA are mainly due to the change in the electrical potential in the pore region due to the decreased dipole moment of phenylalanine. Replacement of Trp by Phe provides a mechanism for tuning the electrostatic environment of the pore. In gramicidin M (gM), all four pairs of Trp are replaced by Phe (Heitz et al., 1982). The electrical potential of the gramicidin pore can also be modified by fluorinating the indole ring (Cotten et al., 1999b). In contrast to the effect of replacing Trp by Phe, 5-fluorination increases the side chain dipole moment according to both experiment (Andersen et al., 1998; Busath et al., 1998; Thompson et al., 2001) and

Submitted July 31, 2001, and accepted for publication May 21, 2002.

Address reprint requests to Dr. Mark F. Schumaker, Dept. of Pure and Applied Mathematics, Washington State University, Pullman, WA 99164. Tel.: 509-335-7273; Fax: 509-335-1188; E-mail: schumaker@wsu.edu.

0006-3495/02/08/880/19 $2.00

computation (Anderson et al., 2001). Lipids also make an important contribution to the electrical potential within the pore interior. De Godoy and Cukierman (2001) report a recent study of this influence on proton conduction through dioxolane-linked gramicidin analogs. Measurements of proton conduction through gA in diphytanoylphosphatidylcholine (Rokitskaya et al., 2002) provide an intriguing comparison with the results in glycerolmonooleate reported here.

The models of proton conduction through gA, gB, and gM described in this work are based on the gA model of Schumaker et al. (2000; 2001). The system simulated by molecular dynamics included a representation of all of the atoms in gA, the pore waters, and a few waters clustered around each channel entrance. The calculations neglected interactions between the channel system and the surrounding lipid and most of the bulk water. Potentials of mean force and diffusion coefficients were calculated for two different sets of simulations. For both sets the reaction coordinate was essentially a scaled axial component of the dipole moment of the pore contents, calculated with respect to the center of the pore. One set of simulations modeled the *occupied* pore; an excess proton was included among 10 pore waters. In this case we designate the axial component of the dipole moment μ^H. The other set of simulations modeled the *empty* pore; the pore contents included only the 10 water molecules, and we designate the axial component of the pore dipole moment μ^d. The superscript d refers to defects in the hydrogen-bonded structure of the water chain that are thought to mediate reversal of the water dipole moments. The potential of mean force (PMF) from the simulations of the occupied pore is designated Φ^H and shown by the dots in Fig. 1 *A*. It has the form of a shallow potential well. In the absence of an applied electrical potential, the excess charge density is concentrated near $\mu^H = 0$, close to the center of the pore. The PMF for the simulations of the empty pore is designated Φ^d and shown as the dots in Fig. 1 *B*. It is dominated by a central barrier centered at $\mu^d = 0$, which we will refer to as the defect or water reorientation barrier. The probability density for μ^d is concentrated near the potential minima, on either side of the defect barrier. The model representation of applied transmembrane potentials Ψ^H and Ψ^d is indicated by the straight lines in Fig. 1, *A* and *B*. The assumption that an applied field is constant within the pore is reasonably accurate for the cylindrical geometry of the gramicidin pore (Jordan, 1982; Roux, 1999). In addition to the potentials shown, diffusion coefficients for the reaction coordinates μ^H and μ^d are obtained from their velocity autocorrelation functions (Schumaker et al., 2000).

These PMFs and diffusion coefficients were incorporated into a configuration space diffusion model of proton conduction through gA. The configuration space is analogous to the state diagram of a rate theory model. Our model does not make the mean field assumption, which is difficult to justify in the context of narrow pores (Hladky, 1999; Miller, 1999; Corry et al., 2000; Moy et al., 2000). The simplified configuration space is shown in Fig. 1 *C*. The top horizontal line segment represents states of the occupied pore and is parametrized by μ^H. The bottom horizontal line segment represents states of the empty pore and is parametrized by μ^d. The two pairs of dashed lines represent two possible sets of transitions between the occupied and empty segments of states; they define the boundary regions on either side of the empty segment. The cartoons at the four corners of the diagram represent extreme states at the ends of the line segments. The channel entrances are designated I and II, as indicated by the cartoon at the lower left. Consider an excess proton entering the channel on side I, at the upper left-hand corner of Fig. 1 *C*. The single-proton model assumes that entry can take place only when channel water dipoles are favorably aligned. As the center of excess charge diffuses through the pore, hydrogen bonds re-form so that the water dipole moments continue to point away from the excess charge. If the excess charge leaves the pore on side II, pore waters are left in an organized state. However, the waters are generally not perfectly aligned, and μ^d will be distributed in some region near the Φ^d potential minimum on side II. The μ^d reaction coordinate must then diffuse over the defect barrier so that the axial component of the pore water dipole moments reverse. Those waters will then be once again aligned to favor proton entry on side I.

This paper presents conductance data for gA, gB, and gM. The gramicidin analogs have dramatically different conduction properties. Consistent with the results of Eisenman et al. (1980), gA has two regimes of current increasing in proportion to concentration, separated by a shoulder between $[H^+] = 0.01$ M and $[H^+] = 0.1$ M. For gB, the shoulder is shifted by approximately half a pH unit in the direction of higher concentrations; gM has currents proportional to concentration from the lowest concentrations measured to $[H^+] > 1$ M. No shoulder is visible in the gM current data. We explain these differences in the conduction properties of the gramicidin analogs as being due to differences in their electrostatic potentials in the pore region. Our model for the electrostatic potential difference between the analogs and gA is inspired by the electrostatic calculation of Anderson et al. (2001). We assume that the difference is constant, independent of the spatial coordinate parallel to the pore axis. We then find that the optimal value of this constant difference is very similar to the result of the electrostatic calculation. However, to obtain this result we have to decrease the amplitude of the water reorientation barrier in gA calculated by the molecular dynamics simulations of Pomès and Roux. A generalization of our result to Trp potentials that vary significantly in the pore interior is outlined in the Discussion.

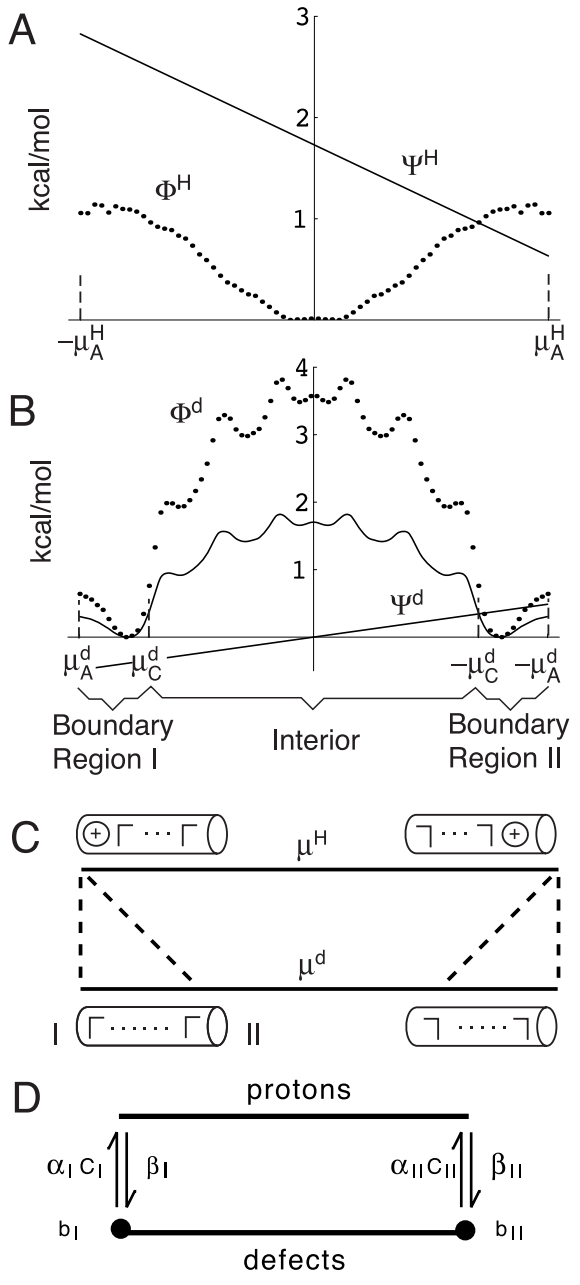

FIGURE 1 (*A*) The intrinsic proton PMF Φ^H is calculated by molecular dynamics (Pomès and Roux, 1997) and the applied PMF Ψ^H corresponds to a transmembrane potential of 150 mV. The reaction coordinate $\mu^H \in [-\mu_A^H, \mu_A^H]$ is the axial component of the dipole moment of the contents of the pore occupied by an excess proton. (*B*) The intrinsic defect PMF is Φ^d and the applied PMF is Ψ^d. The solid curve shows the intrinsic PMF uniformly scaled so that its peak-to-peak amplitude is changed by $\Delta\Delta\Phi^d_{max} = -2.0$ kcal/mol. The reaction coordinate $\mu^d \in [-\mu_A^d, \mu_A^d]$ is the axial component of the dipole moment of the empty pore (occupied only by waters). Boundary states correspond to the regions $\mu_C^d < |\mu^d| < \mu_A^d$. Reorientation of pore waters is believed to be mediated by a packing defect that diffuses through the water column (Phillips et al., 1999; Pomès, 1999). (*C*) Model configuration space of single-proton conduction. The top segment represents the possible proton-occupied states and is parametrized by μ^H. The bottom segment represents the possible empty states and is parametrized by μ^d. Pairs of dashed lines delimit families of possible transitions between the proton and defect segments. They bound boundary regions I and II on the defect segment. (*D*) State diagram of the single-proton model. Boundary regions I and II are lumped into boundary states b_I and b_{II}. The frequencies of transitions between the segments are indicated; α_R and β_R are rate constants, and C_R is the proton concentration on side $R \in \{I, II\}$.

MATERIALS AND METHODS

Experiment

Experimental setup and design was largely described in Phillips et al. (1999) with some exceptions. Single-channel conductance experiments were performed at various concentrations of HCl. Preliminary experiments were conducted using dilutions of 10 N HCl (Fisher Scientific, Fair Lawn, NJ). These experiments were later verified using exact concentrations of 0.9834 N HCl, 0.503 N HCl, 0.1933 N HCl, and 0.1006 N HCl obtained from Aldrich Chemical Company (Milwaukee, WI). Additional experiments were also collected at 0.01 N HCl, 0.02 N HCl, 0.05 N HCl, 0.002 N HCl, and 0.005 N HCl using 10- or 100-fold dilutions of the Aldrich HCl solutions. Experiments collected at 2 N HCl and 5 N HCl were diluted from the 10 N HCl Fisher solution. All dilutions were conducted using distilled water purified to >17.6 MΩ-cm through a Barnstead NANOpure II system (VWR Scientific, San Francisco, CA). The combined data were further verified through direct comparison with the gA data of Eisenman et al. (1980).

Glyceryl monoolein (GMO, NuChek Prep, Elysian, MN) was dissolved in n-hexadecane (50 mg/ml) as described previously (Phillips et al., 1999). N-hexadecane was obtained from three separate sources, specifically from Spectrum Quality Products, Inc. (Gardens, CA, or New Brunswick, NJ), Fisher Scientific, and Aldrich Chemical Company, Inc. The lipid and solvent were used without further purification.

The gA was obtained from ICN Biomedicals (Aurora, OH); gM was prepared by solid-state synthesis using 9-fluroenylmethoxycarbonyl chemistry on an Applied Biosystems model 430a peptide synthesizer (Cotten et al., 1999a). The gM sample was recrystallized and/or repeatedly purified in 95% methanol and 5% water using an octadecylsilane column (Markham et al., 2001); gB was purified from gramicidin D (ICN Nutritional Biochemicals, Cleveland, OH) with an octadecylsilane column using 83% methanol/17% water (Koeppe and Weiss, 1981). Purified peptides were dissolved in HPLC grade methanol (Fisher Scientific) at $\sim 10^{-5}$ mg/ml. Approximately 10–20 pg of peptide were added to 2–3 ml salt baths to obtain the desired frequency of channel formation.

Lipid bilayer membranes were formed and channel conductance performance was measured as described previously (Phillips et al., 1999; Busath et al., 1998). Voltage was applied across the membrane using Ag-AgCl electrodes and a List Medical (Darmstadt, Germany) Patch Clamp L/M-EPC7, or a Warner BC-525C Bilayer Clamp (Warner Instruments, Hamden, CT). The data were collected using voltages between 25 mV and 150 mV at 25 mV increments. Experiments normally lasted between 15 and 40 min. Care was taken to avoid evaporative cooling artifacts. Currents were low-pass filtered at 30 Hz and sampled (100 per second) using a NI-DAQ Data Acquisition Board (National Instruments, Austin, TX) and IGOR Pro Version 3.12 software (Lake Oswego, OR) on a Macintosh computer. Channel conductance was analyzed using TAC X4.1 and TACfit V3.0 (Bruxton Corporation, Seattle, WA). Each experiment contained a minimum of 50 events, and at least three independent experiments were performed at each condition to verify results. Results were temperature-corrected to 23°C, as described by Phillips et al., 1999. Temperature deviations did not surpass 3°C. Data are available in tabular form at http://bioag.byu.edu/zoology/gramicidin. The model calculations described below were also performed assuming $T = 23$°C.

Model

Schumaker et al. (2000, 2001) developed a model of proton conduction through gA based on the molecular dynamics simulations of Pomès and Roux (1997). The latter authors simulated both the diffusion of an excess proton through the pore and the reorientation of water dipole moments in the absence of an excess proton. The reaction coordinates for both simulations can be directly related to the axial component of the dipole moments of the pore contents. The total change in dipole moment was equal to 22.9 e_0 Å. In principle, this result should be equal to an elementary charge passing through the length of the channel. Using the accepted value for the channel length (Urry, 1971; Wallace, 1990) gives $\sim 25 e_O$Å. A possible explanation for the discrepancy is that the proton entrance and exit process were not represented in the simulations.

When the original model with an effective length of 22.9 Å was adapted to a preliminary analysis of the gM data with the electrical distance associated with proton entrance optimized without constraint, a value was obtained that was greater than the total electrical width assigned to the proton entrance and exit steps (Schumaker, unpublished data). However, the analysis is made self-consistent when the channel length is increased to 25 Å and the additional electrical distance assigned to the proton entrance and exit steps. To do this, we begin by distinguishing between the length of the pore, $L_P = 22.9$ Å, and the total length of the channel, $L_T = 25$ Å. Appendix A shows how this distinction can be introduced into the formalism of the framework model (Schumaker et al., 2001) to give a proton conduction model with extended electrical distance.

With the boundary regions shown in Fig. 1 *B*, the original model has a reaction coordinate width of $\mu_A^d - \mu_B^d = 0.55\ e_0$Å associated with proton entrance and exit on either side of the pore. Here, μ_B^d is an effective coordinate of the boundary region on side I (see Appendix A). Physically, this width corresponds to the increased order of pore waters in the presence of an excess proton at an entrance, as compared to the pore waters in the absence of an excess proton. The extended model has a width of $f_E \times e_0 L_T = 1.60\ e_0$Å associated with proton entrance and exit at either side. The new electrical distance f_E includes both the effect of the increased orientation of pore waters and the contribution due to transport of a proton across the physical length of each entrance region.

The original single proton conduction model assigns the full electrical distance f_A^d to the exit rates β_I and β_{II}. This choice assumes that entry into gA is limited by diffusion to the channel mouth and not by a local barrier at the channel entrance. Diffusion into the channel mouth is not very sensitive to an applied electric field, except in the regime of low ionic strength and high applied fields where interfacial polarization becomes important (Andersen, 1983). Similarly, the present model for gA assigns the full electrical distance f_E to the exit rates. However, the models for gB and gM split f_E into two components:

$$f_E = f_N + f_X \tag{1}$$

where f_N is the component of the electrical distance assigned to the entrance step and f_X is the component assigned to the exit step. This allows for the possibility that proton entrance into the channel is limited by a local barrier near the entrance. Entrance rates should then be sensitive to an applied electric field.

As suggested by the calculations of Anderson et al. (2001) we assume that each pair of tryptophans in gA decreases the potential energy of a cation in the pore by a constant, independent of the ion's location along the pore axis. The Trp-11 pair is replaced by Phe in the gB dimer and all four pairs of Trps are replaced by Phe in the gM dimer. We model these replacements by a constant increase in the potential energy of an excess proton in the pore. Let $\Phi^{HZ}(\mu^H)$ be the intrinsic component of the PMF of the proton-occupied gZ pore, where $Z \in \{A, B, M\}$ and μ^H is the proton reaction coordinate. The intrinsic component includes everything except the contribution of the applied transmembrane potential. The energy differences between the gramicidin analogs and gA are denoted by

$$\delta\Phi^Z = \Phi^{HZ}(\mu^H) - \Phi^{HA}(\mu^H) > 0, \tag{2}$$

where $Z \in \{B, M\}$ and $\delta\Phi^B$ and $\delta\Phi^M$ are independent of μ^H. Since we assume the electrical potential energy difference between the analogs and gA is constant, and the empty pore is electrically neutral as a whole, it also follows that

$$\Phi^{dZ}(\mu^d) = \Phi^{dA}(\mu^d). \tag{3}$$

The increased potential energy of an excess proton in the pore of gB or gM has the effect of decreasing the probability of the occupied state as compared with that of gA under the same conditions. The changed probabilities of the occupied state must be reflected in changed values of the mean time before proton entrance into an empty pore and the mean time before proton exit from an occupied pore. Under the assumption that $\delta\Phi^B$ and $\delta\Phi^M$ are constant, these changed mean times must be due to changed rates of proton entrance and exit. To form a mathematical model, we decompose

$$\delta\Phi^Z = \delta\Phi^{NZ} + \delta\Phi^{XZ} \tag{4}$$

where $Z \in \{B, M\}$. $\delta\Phi^{NZ}$ and $\delta\Phi^{XZ}$ determine changes in the entrance and exit rates, respectively. This is described in more detail in Appendix B.

Optimization

Our measure of goodness of fit is χ_r, where the reduced chi-squared error is:

$$\chi_r^2 = \nu^{-1}\Sigma_k (I_k^{SP} - I_k^{Ex})^2/\sigma_k^2. \tag{5}$$

In this equation I_k^{Ex} is the kth experimental current value, I_k^{SP} the corresponding single-proton model current value, and σ_k the experimental standard error of the mean. The number of degrees of freedom is $\nu = N - M$, where N is the number of data points and M is the number of model parameters optimized to fit the data (Press et al., 1992).

Fits of the single-proton model to the gA data are similar to those described by Schumaker et al. (2000). A fixed value of $\Delta\Delta\Phi_{max}^d$ scales the defect PMF, as shown in Fig. 1 *B*. Data at four concentrations ($[H^+] = 2$ mM, 5 mM, 10 mM, and 20 mM) and six voltages ($V_I = 25$ mV, 50 mV, 75 mV, 100 mV, 125 mV, and 150 mV) were used. Values of t^a and ζ were optimized, giving $\nu = 24 - 2 = 22$ degrees of freedom. Fits to the gB and gM data start with the results of the gA analysis. Values of the constant energy differences $\delta\Phi^B$ and $\delta\Phi^M$, defined by Eqs. 2 and 3, are assumed; gB data at five concentrations (from $[H^+] = 2$ mM through $[H^+] = 50$ mM) and six voltages are used for the fit to the gB currents. Values of $\delta\Phi^{NB}$ and f_N^B are optimized, giving $\nu = 30 - 2 = 28$ degrees of freedom. gM data at nine concentrations (from $[H^+] = 2$ mM through $[H^+] = 1$ M) and six voltages are used in the fit to the gM currents. Values of $\delta\Phi^{NM}$ and f_N^M are optimized, giving $\nu = 54 - 2 = 52$ degrees of freedom. In this notation, f_N^Z is the entrance electrical distance for analog $Z \in \{B, M\}$.

Contour plots of χ_r as a function of $\delta\Phi^{NB}$ and f_N^B and χ_r as a function of $\delta\Phi^{NM}$ and f_N^M were examined in several cases, and multiple minima were never found in the physical domain of these parameters. In addition, the smooth variation of χ_r with parameters in Results/Sensitivity Analysis (see below) suggests that the optimized parameters are a smooth function of the assumed fixed values of $\delta\Phi^B$ (or $\delta\Phi^M$) and $\Delta\Delta\Phi_{max}^d$. This suggests that jumps between multiple minima in the $\delta\Phi^{NZ} \times f_N^Z$ plane ($Z \in \{B, M\}$) did not occur in the construction of the sensitivity analysis.

The sensitivity analysis presented in Results determines the values of $\delta\Phi^B$ or $\delta\Phi^M$ and $\Delta\Delta\Phi_{max}^d$ that were fixed in the optimization procedure described above. The optimization procedure was repeated on a grid of different values of $\delta\Phi^B$ or $\delta\Phi^M$ and $\Delta\Delta\Phi_{max}^d$. Intervals of $\Delta\Delta\Phi_{max}^d = 0.25$

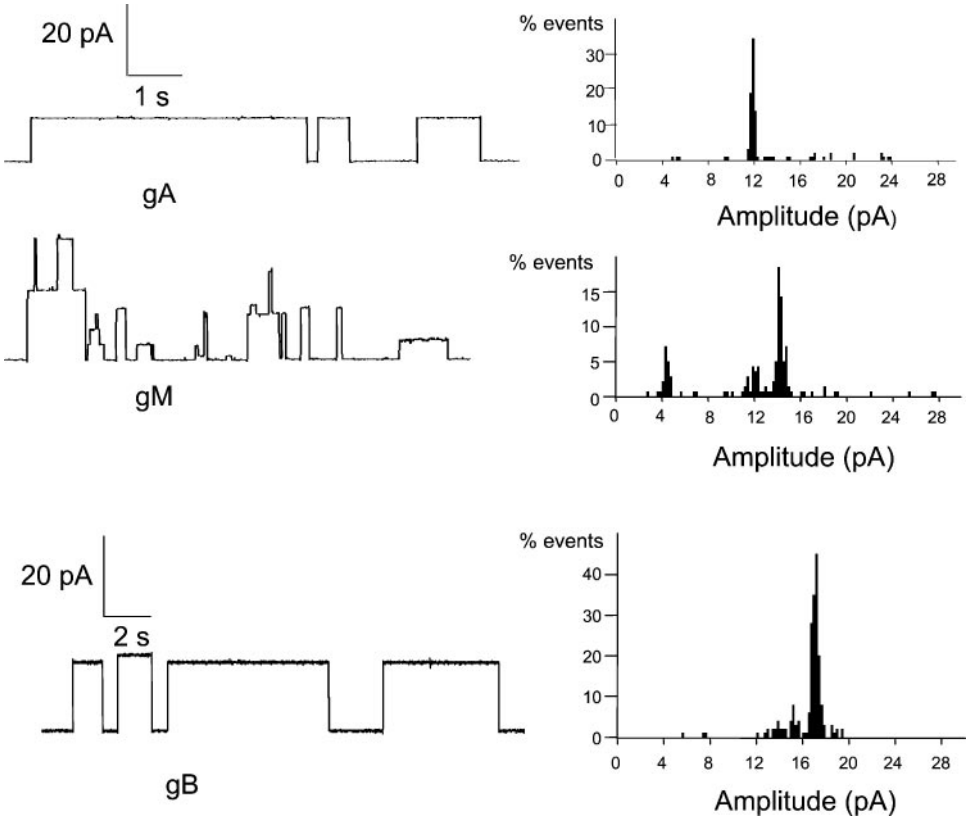

FIGURE 2 Comparison of representative gA, gM, and gB single-channel current traces and conductance histograms from individual experiments. All data were collected in GMO/hexadecane bilayers with 0.1 N HCl solution, 125 mV applied potential, at 21.5°C. At least 50 channels were observed for each experiment, and three or more experiments were performed at each condition. The dominant peak in each histogram was designated the standard conductance for each peptide. The top scale bars refer to the gA and gM current traces and the bottom scale bars to the gB trace.

kcal/mol and $\delta\Phi^B = 0.05$ or $\delta\Phi^M = 0.2$ kcal/mol were chosen. The resulting grid of χ_r values was smoothly interpolated by a third-order polynomial in two variables to give a surface.

RESULTS

Current measurements

Fig. 2 compares gA, gM, and gB single-channel current traces and conductance histograms under identical experimental conditions. The dominant peak in each histogram was designated the standard conductance for each peptide. With gramicidin M there seemed to be more heterogeneity in channel heights than with gA and gB. One consistent nonhomogeneity was a second peak ~30% of the standard peak current. A similar behavior was observed for this peptide previously in alkali metal cation solutions (Markham et al., 2001). For the purposes of this paper we assume that this second peak represents a minor conformational variant that can be ignored. According to our present data and the prior observation of Phillips et al. (1999), channel currents at 50 mV applied potential follow the sequence gA < gB < gM in 0.1 M HCl. This figure shows currents under similar conditions, except that the applied potential is 125 mV. The magnitudes of the currents follow gM ~ gA < gB.

Fig. 3 compares our gA data set with data taken from Eisenman et al. (1980). HCl and HNO_3 proton activities given by Eisenman et al. (1980) were scaled to concentration using the Mathematica package ActivityCoefficients.m developed by Arnd Roth (www.mathsource.com/Content/Applications/Chemistry/0206-198). Fig. 3 *A* shows gA channel current at 50 mV over a large range of $\log[H^+]$. The two sets of data are in good agreement. Both show a shoulder region between 0.01 and 0.1 M. Note that Eisenman et al. (1980) extended their measurements to very low proton concentrations using noise analysis, and found that currents in this regime are proportional to concentration (giving a slope of ~1 on a log-log scale). Fig. 3 *B* shows that the current-voltage relations shift from sublinear to superlinear near the onset of the shoulder just above 0.01 M in both data sets, peaking at 0.1 M and then declining toward 1.0 as saturation is reached. The maximum value of the conductance ratios is obtained at a somewhat lower concentration in our data than in those of Eisenman. In summary, the two data sets show the same qualitative features of current and conductance ratios.

Fig. 4 *A* shows proton currents through gA measured over a wide range of symmetrical proton concentrations, from 2 mM to 5 M, and voltages from 25 mV to 150 mV. In the log-log representation there is a clear shoulder in the gA data with an inflection point at about $\log[H^+] = -1.5$. Above the shoulder there is a second regime with currents approximately proportional to concentration. Finally, for

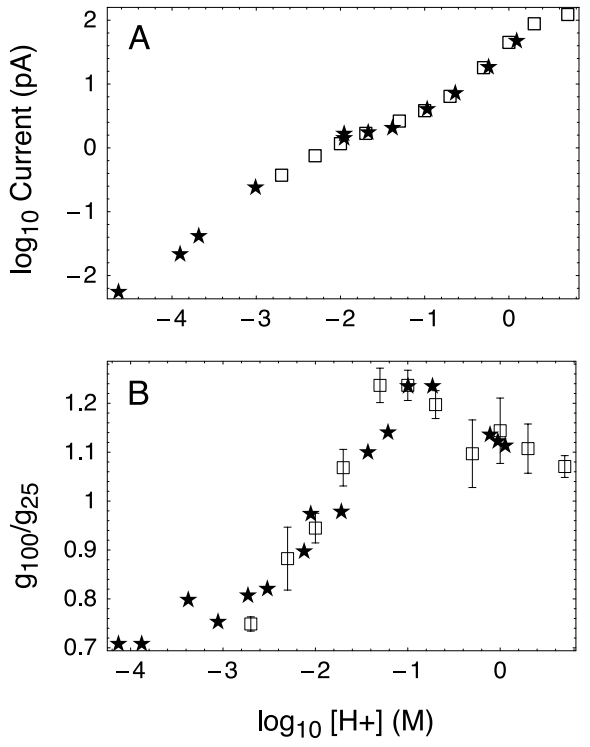

FIGURE 3 Comparison of gA H^+ currents at 50 mV (*A*) and chord conductance ratios (*B*) from previously published (*stars*, taken from Eisenman et al., 1980) and current (*squares*) experiments. Error bars in the current data represent ±1 SEM. In both experiments, bilayers were formed with GMO/hexadecane. The Eisenman et al. (1980) data were taken in the temperature range 22–26°C (see also Neher et al., 1978).

$[H^+] > 1$ M, the rate of increase of conductance with concentration begins to level off.

Fig. 4 *B* shows proton currents through gB measured over the same wide range of concentrations and voltages. The character of these data is generally similar to that of gA, but the shoulder is shifted by ~0.5 pH units, in the direction of higher concentrations. Below the shoulder there is clear convergence to a regime with currents proportional to concentration. The shoulder itself is especially well-defined at low voltages. There is little increase in current between $[H^+] = 100$ mM and 200 mM at 25 mV. Above the shoulder there is again a second regime with currents approximately proportional to concentration. The transition from the shoulder to this second regime is very sharp, similar to observations made by Cukierman on RR dioxolane-linked gramicidin (2000). At concentrations above 1 M the rate of increases of conductance with concentration again levels off.

In comparison with the gA or gB currents, the gM currents shown in Fig. 4 *C* show reduced conductance at low concentrations and a greatly extended regime in which current is proportional to concentration. Similar to the other channels, the rate of increase of conductance with concentration levels off above 1 M. The apparent extension of the low concentration regime as tryptophan is replaced by phenylalanine admits a straightforward interpretation. If the low concentration regime (below the gA and gB shoulders) corresponds to conductance by a single-ion mechanism, and the high concentration regime (above the shoulders) corresponds to a multi-ion mechanism, the transition between these should depend on the electrical potential energy of a cation in the pore. According to all of the estimates (Woolf and Roux, 1997; Dorigo et al., 1999; Anderson et al., 2001) this potential energy should increase in the sequence gA → gB → gM. As the potential energy increases, the probability that the pore is occupied by a cation decreases, and the domain of single ion conductance should extend to higher concentrations.

Fig. 4 *D* compares the current-concentration relationships of gA, gB, and gM at 50 mV applied potential. At 0.002 M, gB (*stars*) starts out at a slightly lower conductance than gA (*triangles*), but then crosses over to a higher conductance at 0.005 M, reaching a shoulder at a higher concentration, and then eventually merging with the gA conductances. At 0.002 M the gM conductance is markedly lower than gA, and crosses over at ~20 mM. It never reaches a shoulder, but above 1 M the rise in conductance tapers off, as it does for the other two peptides. The decline in slope at high concentrations may reflect the same causal factors as with gA and gB. In particular, proton mobility in the bulk may be rate-limiting for $[H^+] > 2$ M (Cukierman, 2000). However, the following discussion of conductance ratios suggests that the gM currents may incorporate a hidden shoulder.

To study the change in *I-V* curve shape with concentration we formed the conductance ratios g_V/g_{25} for $V = 50$ mV, 100 mV, and 150 mV. In this expression, $g_V = I_V/V$ is the chord conductance, where I_V is the current at applied voltage *V*. These ratios are shown in Fig. 5 for each analog and over the full range of concentrations measured. Conductance ratios less than one correspond to sublinear *I-V* curves and ratios >1 correspond to superlinear curves. Fig. 5 *A* shows the ratios for gA. Below the shoulder in Fig. 4 *A* the *I-V* curves are sublinear. There is a transition to superlinearity as $[H^+]$ increases from 5 mM to 50 mM, on the low concentration side of the shoulder. The conductance ratios are approximately linear between $[H^+] = 10$ mM and 20 mM, near the inflection point in the log current versus log$[H^+]$ plot. The ratios attain their maximum values near $[H^+] = 50$ mM and 100 mM (near the point of maximum curvature in the log current versus log$[H^+]$ plot) and then decline at higher concentrations.

Fig. 5 *B* shows the conductance ratios for gB. The general pattern is similar to gA, but is shifted toward higher concentrations by ~0.5 pH units. At low proton concentrations, *I-V* curves are sublinear; values of g_{150}/g_{25} are as low as 0.6. The ratios reverse near $[H^+] = 50$ mM. They attain a well-defined maximum at $[H^+] = 200$ mM, at the same concentration as the very sharp transition to the regime above the shoulder in Fig. 4 *B*. Fig. 5 *C* shows the conduc-

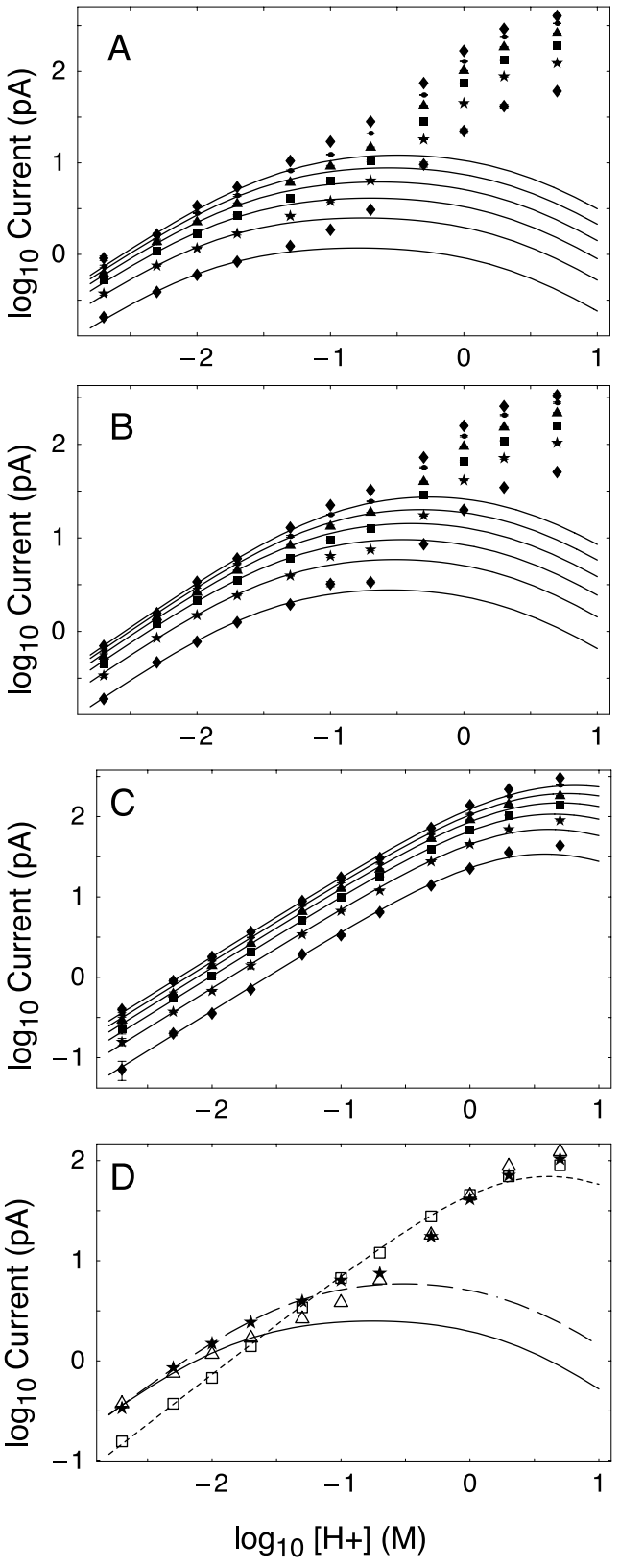

FIGURE 4 Proton currents in symmetrical solutions as a function of $[H^+]$. In the first three panels complete data sets for gA, gB, and gM are shown individually. Applied potentials of measured currents are indicated by symbols (*bottom to top*): 25 mV (*diamonds*), 50 mV (*stars*), 75 mV (*squares*), 100 mV (*triangles*), 125 mV (*circles*), and 150 mV (*diamonds*). Model currents at the respective voltages are indicated by solid curves. Fits by the single-proton model correspond to $\Delta\Delta\Phi^{d}_{max} = -2.0$ kcal/mol; see Fig. 1 *B*. (*A*) Gramicidin A currents. Two parameters controlling the entrance and exit rates are optimized to achieve the fits. Optimized values are $\zeta = 1.959$ kcal/mol and $t^{a} = 21.8$ ns. (*B*) Gramicidin B currents. The parameters $\Delta\Delta\Phi^{d}_{max}$ and $\delta\Phi^{B} = 0.600$ kcal/mol are fixed and the optimized values $f^{B}_{N} \approx 0$ and $\delta\Phi^{NB} = 0.046$ kcal/mol are obtained. (*C*) Gramicidin M currents. The parameters $\Delta\Delta\Phi^{d}_{max}$ and $\delta\Phi^{M} = 3.090$ kcal/mol are fixed and the optimized values $f^{M}_{N} = 0.056$ and $\delta\Phi^{NM} = 0.634$ kcal/mol are obtained. (*D*) Proton currents at the applied potential of 50 mV for gA (*triangles*), gB (*stars*), and gM (*squares*).

tance ratios for gM. There is now a broad domain of sublinear *I-V* curves extending from the lowest concentrations measured to $\sim[H^+] = 1$ M. Compared with the corresponding regime for gB, ratios are not quite as low. g_{150}/g_{25} remains >0.7. Conductance ratios are clearly increasing at $[H^+] = 500$ mM and reverse near 1 M, consistent with the presence of a hidden shoulder.

Preliminary analysis of current measurements

In all three sets of data, *I-V* curves are sublinear at low concentrations and make a transition to superlinearity at a concentration that is fairly well-defined by the data. At sufficiently low concentrations, conductance should be limited by ion entry into the pore. If there is no significant local barrier to ion entry, then entry is limited by diffusion from the bulk to the channel mouth. This process is not expected to be strongly dependent on the transmembrane electrical potential, which would not extend far into the electrolyte solution. Thus, the sublinear *I-V* values at low concentrations can be readily understood. As concentration increases toward the shoulder region of the current data, the *I-V* curves make a transition to superlinearity. Evidently, a voltage-dependent step becomes rate-limiting. As we progress through the sequence gA $\rightarrow$ gB $\rightarrow$ gM, this transition takes place at higher concentrations, corresponding to higher currents and presumably higher proton entry rates. Thus, the data suggest that the voltage-dependent step becomes faster in the sequence gA $\rightarrow$ gB $\rightarrow$ gM. This line of reasoning can be continued to offer some support for the results of Anderson et al. (2001), who concluded that each tryptophan pair lowers the energy of a univalent cation in the pore of gramicidin by $\sim$0.6 kcal/mol. If the onset to superlinearity corresponds to a transition from current limited by entry to current limited by a step taking place within the channel, then it should also correspond to rapidly increasing probability that the channel, as a whole, is occupied by a proton. This suggests that the proton concentration at the onset to superlinearity will be close to the proton dissociation constant. Let K_Z be the proton association constant and let ΔE_Z be the difference between the energy of a proton in the channel and the energy of an empty channel in

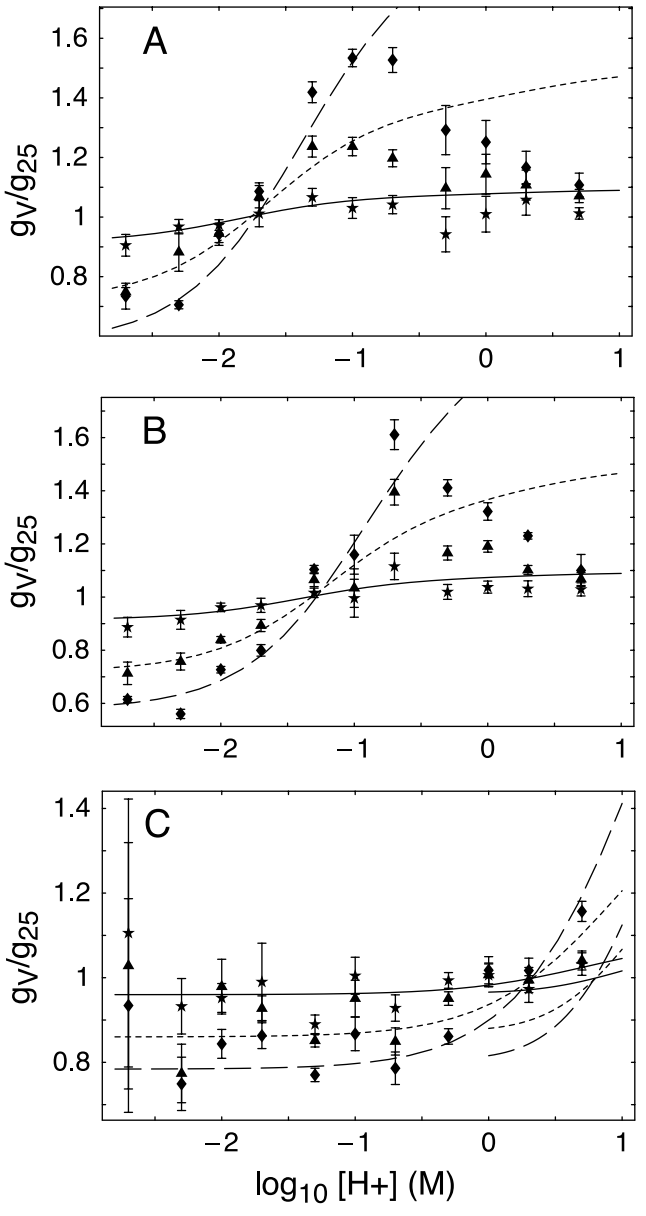

FIGURE 5 Conductance ratios g_V/g_{25} formed from proton conductances in Fig. 4. Symbols designate *V*: 50 mV (*stars*), 100 mV (*triangles*), and 150 mV (*diamonds*). Model conductance ratios are indicated by curves: 50 mV (*solid*), 100 mV (*short dash*), and 150 mV (*long dash*). (*A*) Gramidicin A. (*B*) Gramicidin B. (*C*) Gramicidin M. In *C*, thin lines indicate conductance ratios for a model fit assuming $\Delta\Delta\Phi^{d}_{max} = -1.25$ kcal/mol.

combination with a proton in bulk solution (Z = A, B or M). We should then have

$$K_Z = \frac{[H^+ gZ]}{[H^+][gZ]} \propto \exp(-\beta\Delta E_Z), \tag{6}$$

and, as a consequence

$$K_M = K_A \exp(-\beta\delta\Phi^M), \tag{7}$$

where $\delta\Phi^M = \Delta E_M - \Delta E_A$, according to the notation introduced by Eq. 2. Approximating the proton dissociation constant with the proton concentration at the onset of superlinearity (these estimates are consistent with model calculations, see Eq. B14), we have from Fig. 5 that $K_M^{-1} \approx 1$ M and $K_A^{-1} \approx 10$ mM. From Eq. 7 we then have $\delta\Phi^M \approx 4.6k_BT \approx 2.7$ kcal/mol. The average cation energy contribution per tryptophan pair is then ≈0.7 kcal/mol, in rather good agreement with the results of Anderson et al. Fig. 5 *B* suggests that $K_B \approx 30$ mM, with the result that $\delta\Phi^B = \Delta E_B - \Delta E_A$ is about one-quarter of $\delta\Phi^M$. This would mean that the potential energy contribution of the Trp-11 pair is close to the average contribution per Trp pair, in further agreement with the results of Anderson et al.

We tentatively identify the domain of increasing conduction above the shoulders in Fig. 4, *A* and *B* with the onset of significant multi-proton conduction. This identification is consistent with our interpretation of the onset of superlinearity in Fig. 5, *A* and *B* as signifying rapidly increasing probability of single proton occupation of the gramicidin pore. The increase in occupation probability satisfies a pre-condition for multi-proton conduction, which requires ion entry into an already occupied channel. However, DeCoursey and Cherny (1999) have argued that the defect in the hydrogen-bonded chain that would necessarily exist between two excess protons in the pore would slow the rate of conduction below that observed experimentally. It would be very interesting to have molecular dynamics simulations of the multiply occupied pore, especially if the entrance and exit processes could be studied.

Single-proton model fits to current data

This section describes the fits of the extended single-proton model of gramicidin conduction to the current measurements of gA and its analogs shown in Fig. 4. The model is based on that described by Schumaker et al. (2000, 2001) but modified by increasing the effective length of the channel from 22.9 Å to 25 Å and assigning the difference to the channel entrance regions, as described in Methods and Appendix A. As suggested by the calculations of Anderson et al. (2001), we assume that each Trp pair makes a constant contribution to the electrical potential energy of a cation in the pore, independent of the spatial coordinate z parallel to the pore axis. The corresponding model variables are $\delta\Phi^B$ and $\delta\Phi^M$ (see Eq. 2); these are the positive energy differences between the proton-occupied states of the analogs and gA. The assumption that the contribution of the Trps is constant greatly simplifies the model, making the results independent of the detailed distribution of charge in the pore. The energy of interaction of the pore contents with the charge distribution of the indole ring system depends only on the net charge of the pore, which is +1 when the pore is occupied by an excess proton and 0 when the pore is only occupied by waters.

To obtain good fits to the gB and gM data it is necessary to reduce the height of the water reorientation barrier cal-

culated by the molecular dynamics simulations of Pomès and Roux (1997). The original barrier is shown as the dots in Fig. 1 *B*. The present analysis assumes that the intrinsic potential Φ^d is uniformly scaled so that its maximum peak-to-peak amplitude is reduced by $\Delta\Delta\Phi^d_{max} = -2.0$ kcal/mol. This scaled profile is shown as a solid curve in Fig. 1 *B*. The sensitivity analysis below gives an overview of how model fits depend on $\Delta\Delta\Phi^d_{max}$.

To achieve the fits to the gA data shown in Fig. 4 *A*, two parameters controlling the proton entrance and exit rates are optimized, holding the description of proton transport through the interior of the channel fixed. Proton entrance is assumed to be independent of applied potential, therefore all of the electrical distance associated with the channel entrances was assigned to the proton exit step. Only the data presented in Fig. 4 *A* between 2 mM and 20 mM were used in the fit, because currents too close to the shoulder might include a significant contribution due to multi-ion conduction. At each concentration, currents at all six voltages were used in the optimization. The agreement is good, except for some points at 125 mV and 150 mV. The variables that were optimized are ζ and t^a; ζ is equal to $\Phi^d(\mu^d_C) - \Phi^H(\mu^H_A)$ plus a term that is proportional to the logarithm of the pore volume (Schumaker et al., 2001). t^a controls the proton exit rate (see Eqs. A15 and A16) and also determines the time scale of the mean time before exit (Appendix C). Together, ζ and t^a control the proton entrance rate (see Eqs. A13 and A14). Optimized values of ζ and t^a are given in the legend to Fig. 4.

Model currents in Fig. 4 *A* increase to a maximum value for $[H^+]$ between 100 mM and 500 mM, and then decline due to the clogging mechanism (Schumaker et al., 2000). To understand the clogging mechanism, consider an excess proton leaving the occupied pore on side II (Fig. 1 *C*). The waters of the empty pore must reverse their dipole moments before another proton can enter from side I. If the mean time required for proton entry on side II is shorter than the time required for water reorientation, a proton is most likely to re-enter the pore from side II. This frustrates the cycling around the diagram required for proton transport through the pore. Clogging reflects the finite rate of water reorientation and disappears as this rate is taken to infinity.

The fits to the gB and gM data shown in Fig. 4 use the gA analysis as a starting point. We assume a value for $\delta\Phi^Z$, $Z \in \{B, M\}$, the constant difference between the energy of a cation in the pore of the analog and gA. Then two variables are optimized to make the fit to each analog. The first is the component of $\delta\Phi^Z$ that alters the entry rate, $\delta\Phi^{NZ}$ (see Eq. 4), and the second is the electrical distance associated with proton entrance, f^Z_N.

The fit to the gB current data in Fig. 4 *B* is based on all of the data up through $[H^+] = 50$ mM; $\delta\Phi^B$ is the increase in energy of a cation in the pore of gB relative to gA. From the sensitivity analysis (presented below) this is fixed at the value $\delta\Phi^B = 0.600$ kcal/mol. This value is optimal for $\Delta\Delta\Phi^d_{max} = -2.0$ kcal/mol under the additional constraint that $f^B_N \geq 0$. It is in very close agreement with the calculations of Anderson et al. (2001). Optimized values of $\delta\Phi^{NB}$ and f^B_N are given in the figure legend. The rate of entrance into gB is only ~8% less than the rate into gA. The electrical distance associated with entrance into gB is zero. The interpretation is that there is no significant activation barrier for proton entrance into gB and (consistently) the associated electrical distance is zero. One also obtains that the model gB exit rate is ~2.6 times the gA exit rate. In summary, our model results suggest that gB and gA share the property that there is no significant local barrier at the channel entrance to the entry of an excess proton into the empty channel. The difference between the conductance properties of the gB and gA models is almost entirely due to an increased rate of proton exit from the gB pore.

The fit to the gM current data in Fig. 4 *C* is based on all of the data up through $[H^+] = 1$ M; $\delta\Phi^M$ is the increase in the energy of a cation in the pore of gM, relative to gA, due to the replacement of all four Trp pairs with Phe. From the sensitivity analysis, the value $\delta\Phi^M = 3.090$ kcal/mol was fixed; this is optimal for $\Delta\Delta\Phi^d_{max} = -2.0$ kcal/mol. Note that $\delta\Phi^M \approx 5\delta\Phi^B$. Optimized values of $\delta\Phi^{NM}$ and f^M_N are given in the figure legend. The result for $\delta\Phi^{NM}$ implies that the model gM entrance rate decreased by a factor of ~2.9, compared with the entrance rate into gA. Formally, this factor corresponds to an entrance barrier of ~1 *kT*. The associated reaction coordinate width assigned to the entrance step, $f^M_N \times e_0 L_T = 1.41 e_0$Å, is only a little less than the total width, $f_E \times e_0 L_T = 1.60\ e_0$Å, assigned to the entrance region. The value of $\delta\Phi^{XM}$ obtained from Eq. 4 implies that the model gM exit rate is ~65 times the gA exit rate. To summarize, the model representation of gM includes substantially slowed entrance and much faster exit compared to gA or gB. Furthermore, the proton entrance process is voltage-dependent in gM, but not in gA or gB.

Comparison of model and experimental conductance ratios

Fig. 5 compares the observed conductance ratios with the proton conduction model. Values of the model parameters were obtained by optimizing the fit with the current data in Fig. 4 as described above. Model ratios were not directly optimized to fit observed ratios. The gA model ratios are compared with observed ratios in Fig. 5 *A*. The observed ratios are somewhat scattered; the process of forming g_V/g_{25} leads to a significant standard error, especially at low concentrations. However, the model is in general agreement with the trend of the data below the proton concentration at which the conductance ratios reverse, ~20 mM. The low values of the model ratios in this regime (<1.0) are due to the rate-limiting entrance step, which does not depend on applied voltage. Model ratios continue to follow the observations to the maximum at $[H^+] = 100$ mM, well above the

highest concentration used in the optimization procedure. However, the model ratios fail to follow the subsequent decline in the observed ratios, as the model fails to follow the secondary rise in Fig. 4 *A*.

Fig. 5 *B* shows a particularly nice comparison between the observed and model gB current ratios below the concentration where the ratios reverse. Model ratios reverse for $[H^+]$ near 50 mM, in good agreement with the data. However, they do not quite match the very sharp increase in the observed ratios to a maximum at 200 mM. In Fig. 5 *C*, model gM ratios for $\Delta\Delta\Phi^{d}_{max} = -2.0$ kcal/mol are the thick curves extending across the figure. These are in general agreement with the data for $[H^+] \leq 500$ mM. In particular, the model ratio g_{150}/g_{25} saturates at a minimum level of $\sim$0.8. This increase as compared to the model ratios g_{150}/g_{25} for gA and gB is due to the voltage-dependent entrance rate. However, the experimental conductance ratios for gM reverse near $[H^+] = 1$ M, while the model ratios reverse near $[H^+] = 2$ M. Model ratios for $\Delta\Delta\Phi^{d}_{max} = -1.25$ kcal/mol and the corresponding optimal value of $\delta\Phi^{M}$ are shown as thin curves for $[H^+] \geq 1$ M. These reverse for a value $[H^+] > 5$ M, clearly different from the experimental result.

Times required by the individual kinetic steps

Next, consider the times for the individual kinetic steps involved in the process of proton permeation from side I to side II according to the single-proton model. Suppose that a positive applied voltage $V_I > 0$ gives a net current of protons from side I to side II. Beginning at the upper left-hand corner of the state diagram in Fig. 1 *D*, the kinetic steps in the direction of the current are as follows. 1) The mean time t_X for a proton to exit the channel starting from just inside the channel entrance at side I. 2) The mean time t_R for a defect in an empty channel, starting at state b_{II}, to cross over the water reorientation barrier and reach state b_I. We calculate this with the possibility of the proton entering the channel on side II neglected. 3) The mean time t_N for a proton to enter the channel on side I, assuming that it remains in state b_I until that time. We denote the sum of these mean times by t_S. As the applied voltage on side I becomes large, the mean time for a proton to permeate the channel should approach t_S. In Fig. 6 we compare t_S with the current time, denoted t_C, which is simply the reciprocal of the current from side I to side II (the current in units of ions per nanosecond). An applied voltage of $V_I = 150$ mV was used to construct the figure. The times given correspond to the fits to the gA, gB, and gM data presented in Figs. 4 and 5. In particular, the water reorientation barrier shown in Fig. 1 *B* is uniformly scaled so that its amplitude is reduced by 2 kcal/mol.

Fig. 6 *A* shows the different times for gA. At the lowest concentrations, near $[H^+] = 1$ mM, the model current is limited by the entrance process. We may call this the

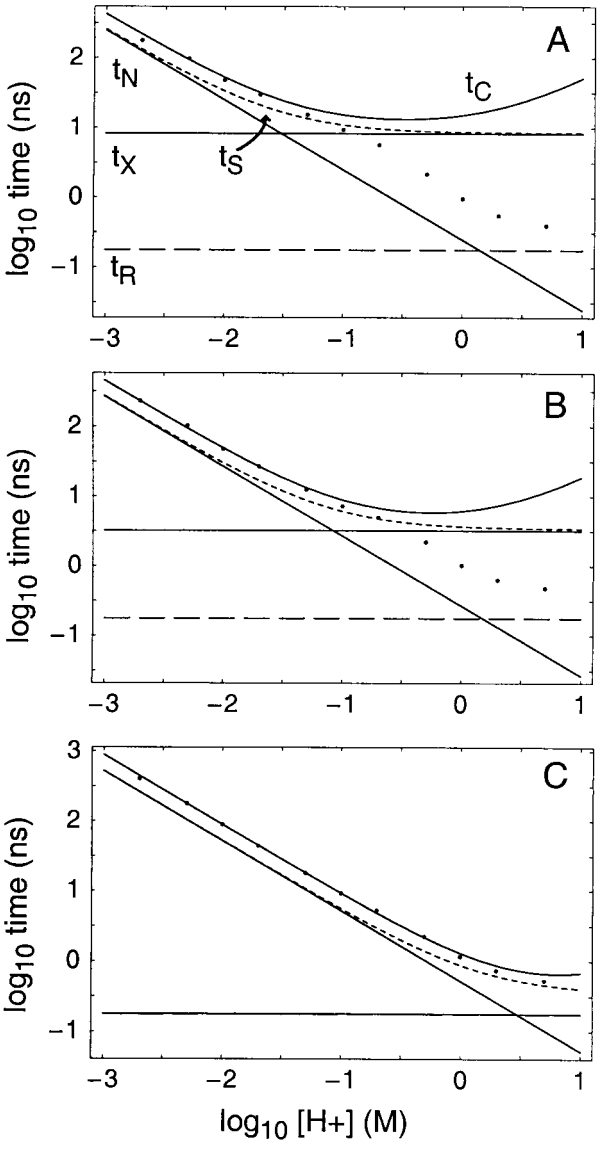

FIGURE 6 Times for individual kinetic steps in the model fit of Fig. 4. The applied potential is fixed at 150 mV. (*A*) Gramicidin A. From bottom to top and to the left of all crossover points, curves represent the water reorientation time t_R (*long dash*), the exit time t_X (*solid*), the entrance time t_N (*solid*), the sum $t_S = t_R + t_X + t_N$ (*short dash*), and the model current time t_C (*solid*). Dots represent experimental current times. (*B*) Gramicidin B. (*C*) Gramicidin M. In the last panel $t_R \approx t_X$.

entrance-limited regime. At moderate applied voltages t_C is substantially greater than $t_S \approx t_N$, because there is a significant probability that kinetic steps will take place in the direction opposed by the applied field. For example, an ion that has just entered the channel from side I may exit the channel on the same side. At very large applied voltages, t_C approaches t_N; and the current becomes more nearly diffusion-limited (results not shown). As concentration increases, t_N decreases in proportion to $[H^+]^{-1}$; t_N and $t_X$cross near $[H^+] = 30$ mM, at the low concentration side of the

shoulder in Fig. 4 *A*. At slightly higher concentrations, the experimental values of the current time depart the model curve. This corresponds to the second regime of current proportional to concentration in Fig. 4 *A*. Throughout the concentration range, model reorientation times are much shorter than exit times.

The figure for gB is similar to that for gA, except that t_N and t_X cross near $[H^+] = 80$ mM, at the low concentration side of the shoulder in Fig. 4 *B*. The gap between the exit and reorientation times is somewhat decreased as compared to that for gA, but these times are still well-separated. Fig. 6 *C* shows that the model representation for gM is entrance-limited for concentrations much below 1 M. The exit and reorientation time scales are now very nearly equal.

Spatial dependence of the mean time before exit

The mean time before exit t_X described in the previous section combines translocation across the pore interior with exit. However, the proton translocation process is itself very fast, due to the very high proton diffusion coefficient calculated by molecular dynamics (Schumaker et al., 2000) and the absence of a barrier in the proton PMF. The high proton translocation rate is apparent from Fig. 7, which shows the spatial dependence of the mean time before exit, $\bar{t}(z)$, for gramicidin A and the analogs; z is the spatial coordinate parallel to the pore axis. Appendix C describes how $\bar{t}(z)$ is calculated. Values of t_X correspond to $\bar{t}$ evaluated at the left-hand endpoint of the curves in Fig. 7. The figure compares $\bar{t}(z)$ for gA in the absence and presence of an applied potential, as well as comparing $\bar{t}(z)$ for gA, gB, and gM in the presence of an applied potential. If the scale on these graphs were changed so that the base of the ordinate were $\bar{t} = 0$, the graphs would all look nearly flat. The mean first passage time to escape the channel depends only slightly on the initial value of z within the channel. This reflects the different time scales to diffuse across the pore and to escape. According to the diffusion coefficient calculated from the molecular dynamics simulations (Schumaker et al., 2000), transport of the center of excess charge along a column of properly aligned water molecules is very fast. The mean time to leave the channel is much longer. As a consequence, model trajectories diffuse across the length of the pore many times before finally exiting. Fig. 6 *A* of Schumaker et al. (2000) gives a short segment of a typical trajectory.

Although they are nearly flat, the mean first passage time curves shown in Fig. 7 provide insight into the proton conduction model. We first consider the case of zero applied potential, $\Psi_I = 0$. Fig. 7 *A* shows the corresponding $\bar{t}(z)$. It is slightly higher in the middle of the pore, as would be expected. The mean times before exit are shorter for gB and gM, but the shape of their

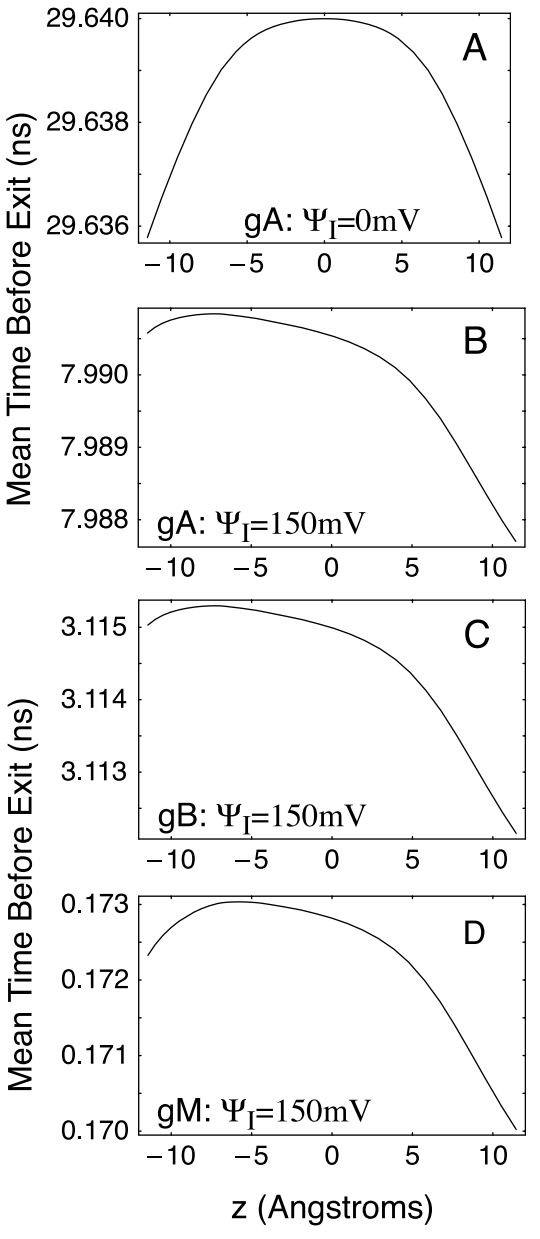

FIGURE 7 Mean time before proton exit as a function of the coordinate z parallel to the pore axis. (*A*) Gramicidin A, $\Psi_I = 0$. (*B*) Gramicidin A, $\Psi_I = 150$ mV. (*C*) Gramicidin B, $\Psi_I = 150$ mV. (*D*) Gramicidin M, $\Psi_I = 150$ mV.

functions $\bar{t}(z)$ are identical to that of gA (see Appendix C/Solution; figures not shown). For gB, $\bar{t}(-\mu_A) = 11.5$ ns and for gM, $\bar{t}(-\mu_A) = 0.454$ ns. Fig. 7, *B–D* show $\bar{t}(z)$ when $\Psi_I = 150$ mV and $\Psi_{II} = 0$ mV. The main effect of an applied potential is to markedly decrease the mean time before a proton exits the channel; $\bar{t}(z)$ is a decreasing function over most of the pore, reflecting the large probability of exit through side II. While the shape of $\bar{t}(z)$ is no longer identical for the analogs, differences are small for the examples shown.

Sensitivity analysis

In this section we explore the quality of the single proton model fits as a function of our assumptions concerning the height of the water reorientation barrier and the constant contribution to the proton PMF due to the replacement of Trps by Phes. The optimization procedure is described in Methods/Optimization. The criterion for goodness of fit is χ_r, defined by Eq. 5. Fits to the gA data (for which we show no sensitivity plot), depended on the value of $\Delta\Delta\Phi^d_{max}$, which gives the change in the peak-to-peak amplitude of the defect PMF, as shown in Fig. 1 *B*. For the potential computed by molecular dynamics (Pomès and Roux, 1997), corresponding to $\Delta\Delta\Phi^d_{max} = 0$, $\chi_r = 3.35$. This decreases to a soft minimum near $\Delta\Delta\Phi^d_{max} = -1.75$ kcal/mol, with a value of $\chi_r = 2.83$. The error then increases very slightly to a value of $\chi_r = 2.87$ at $\Delta\Delta\Phi^d_{max} = -2.5$ kcal/mol, corresponding to the lowest defect potential barrier considered. As described in Materials and Methods/Model, the gA model assumes there is no local barrier to proton entry at the channel entrance, and the electrical distance associated with entrance is also zero.

To carry out the sensitivity analyses for gB or gM we consider the goodness-of-fit χ_r as a function of two parameters that were fixed during optimization, $\Delta\Delta\Phi^d_{max}$ and the energy difference $\delta\Phi^B$ or $\delta\Phi^M$ between the proton potential in the analog and gA; see Eq. 2. The construction is described in Materials and Methods. Contour maps of the χ_r surface are given by Fig. 8, *A* and *B*. On the abscissas are $\delta\Phi^B$ or $\delta\Phi^M$ and on the ordinates is $\Delta\Delta\Phi^d_{max}$. Solid contours correspond to constant values of χ_r as indicated by the accompanying numerals.

For gB (Fig. 8 *A*), optimal fits require that $\delta\Phi^B$ fall between 0.5 and 0.6 kcal/mol and that $\Delta\Delta\Phi^d_{max} < -1.5$ kcal/mol. The long-dashed curve indicates the loci of values at which the entrance electrical distance $f^B_N = 0$. To the left of this curve, f^B_N has unphysical negative values. However, these negative magnitudes are very small, as indicated by the short-dashed curves which indicate $f^B_N = \pm 0.01$. A value of $f^B_N = 0.01$ corresponds to an elementary charge moving across 1% of the pore length, or 0.25 Å. The curve $f^B_N = 0$ is close to the innermost contour, $\chi_r = 3.1$. Values of χ_r are between 3.0 and 3.1 within this contour. The proximity of this contour with the curve $f^B_N = 0$ suggests that a value of $f^B_N \approx 0$ should be assigned to gB, and that $\delta\Phi^B \approx 0.6$ kcal/mol, in excellent agreement with the results of Anderson et al. (2001). The dot with coordinates $\delta\Phi^B = 0.600$ kcal/mol and $\Delta\Delta\Phi^d_{max} = -2.0$ kcal/mol has $f^B_N \approx 0$, $\delta\Phi^{NB} = 0.046$ kcal/mol, $\chi_r \approx 3.04$, and corresponds to the model analysis given in Fig. 4 *B*.

For gM (Fig. 8 *B*) the optimal $\delta\Phi^M$ is constrained to a narrow range of 2.9–3.1 kcal/mol. The long-dashed curve indicates $f^M_N = f_E = 0.064$, the full electrical distance available to entrance or exit. The physically accessible region ($f^M_N < f_E$) is below and to the left this curve. The short-dashed curve corresponds to $f^M_N = f_E - 0.01$. The inner contour corresponds to $\chi_r = 3.5$. Values as low as $\chi_r \approx 3.4$ are achieved within this band. Parameter values of

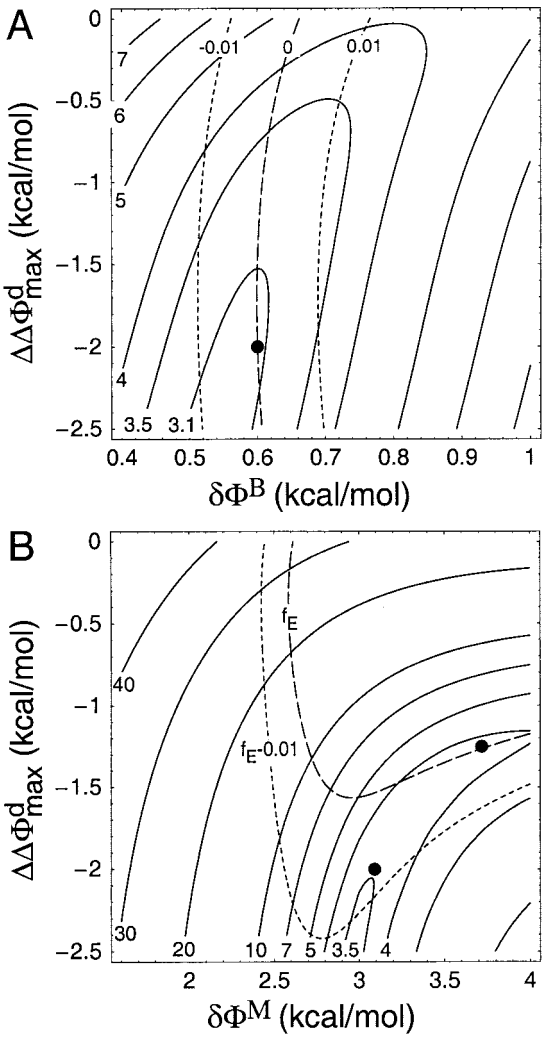

FIGURE 8 Sensitivity analysis of single-proton model fits to currents in Fig. 4, *B* and *C*. $\delta\Phi^Z$, $Z \in \{B, M\}$, is the constant difference in the intrinsic proton PMF between gZ and gA. $\Delta\Delta\Phi^d_{max}$ is the change in the amplitude of the defect PMF defined in Fig. 1 *B*. Each point in the field corresponds to a fit of the single proton model to the data with $\delta\Phi^Z$ and $\Delta\Delta\Phi^d_{max}$ fixed and values of $\delta\Phi^{NZ}$ and f^Z_N optimized. $\delta\Phi^{NZ}$ is the activation energy and f^Z_N is the electrical distance associated with proton entrance. Solid contours correspond to constant χ_r, where χ^2_r is defined by Eq. 5. Values of χ_r are indicated by numerals on the curves. Long and short dashed contours correspond to constant values of f^Z_N, whose values are indicated on the curves. (*A*) Sensitivity analysis of gB fits. Fits giving negative electrical distance, to the left of the long-dash contour, are not physical. The dot with coordinates (0.600, −2.0) corresponds to the fit presented in Fig. 4 *B* and to Fig. 5 *B*. (*B*) Sensitivity analysis of gM fits. Fits giving $f^M_N > f_E$ are not physical; these are enclosed by the long-dash contour in the upper right quadrant of the field. The dot with coordinates (3.040, −2.0) corresponds to the fit presented in Fig. 4 *C* and to the curves extending across the width of Fig. 5 *C*. The dot with coordinates (3.718, −1.25) corresponds to the thin curves in Fig. 5 *C*.

the two model analyses shown in Fig. 5 *C* are given as dots in Fig. 8 *B*. The dot with coordinates $\delta\Phi^{M} = 3.090$ and $\Delta\Delta\Phi^{d}_{max} = -2.0$ kcal/mol has $\chi_r \approx 3.50$, and corresponds to the thick lines that extend across the width of Fig. 5 *C*. This parameter set is also analyzed in Fig. 4 *C*. The dot with coordinates $\delta\Phi^{M} = 3.72$ and $\Delta\Delta\Phi^{d}_{max} = -1.25$ kcal/mol has $\chi_r \approx 3.88$ and corresponds to the thin lines in Fig. 5 *C*, which is less a desirable fit because the current ratios reverse at concentrations that are clearly higher than those of the measurements. Fits to these data with significantly greater values of $\Delta\Delta\Phi^{d}_{max}$ give the unphysical result $f^{M}_{N} > f_E$. We conclude from the sensitivity analysis of the gM data that $\Delta\Delta\Phi^{d}_{max} \leq -1.5$ kcal/mol. The sensitivity analysis suggests that $\delta\Phi^{M} \approx 3$ kcal/mol, slightly greater than the total contribution to the electrical potential energy within the pore due to replacing all four Trp pairs in gA with Phe as calculated by Anderson et al. (2001).

For gM there appears to be a significant barrier to proton entrance. This differs from the situation for gB. For the dot in Figure 8 *B* corresponding to $\Delta\Delta\Phi^{d}_{max} = -2.0$ kcal/mol, the entrance reaction coordinate width is almost 90% of f_E and corresponds to the displacement of an elementary charge through 1.4 Å. Apparently, however, this value is significantly less than f_E. The spatial dependence of the mean first passage time for proton escape presented in Fig. 7 *D* shows that model trajectories of protons in the pore of gM reflect with high probability at the channel entrances, consistent with the existence of a significant barrier to proton exit, as is the case for gA and gB.

Rate constant representation profile

Fig. 9 shows hybrid PMF/rate constant representation profiles (Andersen, 1999) for gA, gB, and gM in the GMO bilayer environment, based on the single-proton model fits shown as the solid curves in Fig. 4, *A–C*, and Fig. 5. In the entrance regions ($\mu > \mu^{H}_{A}$ and $\mu < -\mu^{H}_{A}$) the profiles represent the energies and electrical distances of the optimized fits to the conductance data. This representation is much like an energy profile from rate theory and is called a rate constant representation profile by Andersen (1999). The total width, ~19 e_0Å, corresponds to the sum of the dipole moment displacement associated with proton transport in the molecular dynamics simulations (Fig. 1 *A*) and the displacement associated with proton entrance and exit.

Based on previous results, we assume that there is no significant barrier for proton entrance into gA (Schumaker et al., 2000), and the present analysis suggests that the corresponding barrier to entrance into gB is also negligible. However, we found a significant barrier into gM corresponding to $\delta\Phi^{NM} = 0.634$ kcal/mol, and this is represented in the figure. Absolute energies for protons in the pore represent the extent to which protons are concentrated in the pore relative to bulk solution in the limit of low excess proton concentrations. Appendix B discusses the construction of this figure in more detail. The model translocation step is not rate-limiting due to the high diffusion coefficient of the proton within the channel, so the model analysis presented in this paper says little about the accuracy of the proton PMF shape.

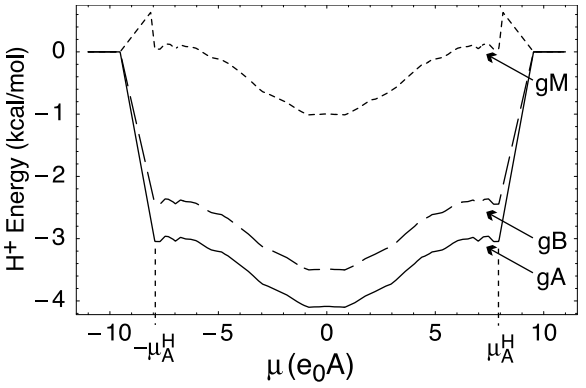

FIGURE 9 Hybrid proton PMF/rate constant representation profile for proton conduction through gA, gB, and gM. The extended reaction coordinate μ corresponds to μ^{H} in the interior of the pore ($-\mu^{H}_{A} < \mu < \mu^{H}_{A}$). Outside the interior, the profile represents optimized values of energies and electrical distances associated with proton entrance and exit in the spirit of rate constant representation. These optimized values correspond to the fits shown in Figs. 4 and 5. In the interior, the profile is the sum of the proton PMF calculated by molecular dynamics (Fig. 1 *A*) and the potential differences due to replacing Trps by Phes in the analogs gB and gM.

DISCUSSION

Fig. 4 shows that the replacement of the gA Trps by Phes in gB and gM leads to dramatic changes in the conductance properties of these channels. We propose a very simple explanation for these measurements: replacement of Trps by Phes increases the electrical potential of cations in the pore. This lowers the pore occupancy probability and greatly extends the domain of concentrations over which the pore is occupied by at most one cation at a time. The fact that such changes in conductance properties can be explained on the basis of a through-space electrostatic interaction with the Trp indoles, located 7 or 8 Å from the pore axis, emphasizes the detail and precision that computer simulations need to achieve before they can accurately predict the conductance properties of ion channels.

We have assumed that the replacement of each pair of Trps by Phes in the analogs contributes a constant to the potential energy of a cation in the pore. A constant shift in potential energy does not change the shape of the proton PMF, so a change in pore occupancy probability must be reflected by a change in entrance and exit rates. We have interpreted the ~100-fold increase in the concentration at which gM conductance ratios reverse (compared to gA) as being due to a combination of slower proton entrance and faster proton exit. The magnitudes of the Trp potential

contributions for gB and gM are in very good agreement with electrostatic computations (Anderson et al., 2001).

This mechanism can be generalized to consider Trp potentials that vary in the pore interior. Define the mean time the channel is *occupied*, t_O (the time between the exit of an excess proton and the previous entrance) and the mean time *empty*, t_E (the time between an entrance and the previous exit). Then one may see that

$$t_O/t_E = Q^H/Q^d \quad (9)$$

At thermodynamic equilibrium, the ratio of the occupied to empty pore probabilities is given by a ratio of integrals of Boltzmann factors over the pore interior (see Eq. B2). According to each of the three available calculations (Woolf and Roux, 1997; Dorigo et al., 1999; Anderson et al., 2001) the Trp indole dipole stabilizes cations in the pore interior, increasing the ratio Q^H/Q^d. Then substituting Trp → Phe must decrease this ratio, which may be achieved by slowing proton entrance (increasing t_E), speeding proton exit (decreasing t_O) or both.

Becker et al. (1991) measured currents through gramicidin and several Trp → Phe analogs at 1 M symmetrical Na^+. They found that conductance decreases as the number of Trps replaced by Phe increased. This result suggests that replacement of Trp by Phe increases the Na^+ translocation barrier (Becker et al., 1992; Hu and Cross, 1995). Experiments with fluorinated derivatives of Trp also suggest that gA conductance at high symmetrical [Na^+] is limited by a translocation barrier (Thompson et al., 2001). These results seem inconsistent with the nearly constant Trp potential of Anderson et al. (2001), which would imply that the Trps enhance Na^+ binding without affecting translocation. The Becker et al. finding and Hu and Cross interpretations seem more consistent with the unimodal Trp energy profile found by Dorigo et al. (1999), which would decrease the height of the Na^+ translocation barrier. The bimodal potential profiles of Woolf and Roux (1997) could also be qualitatively consistent with the results of Becker et al. However, the rate theory modeling of Thompson et al. (2001) demonstrated that the Anderson et al. potential profile for 5F-Trp, when compared to the flat potential for native Trp, adequately predicted the Na^+ and K^+ conductance enhancements seen when Trp-13 is fluorinated in gA. Further work is necessary to distinguish between the shapes of these potential profiles with confidence.

If the potential profile shapes calculated by Woolf and Roux (1997) or Dorigo et al. (1999) are more accurate than that of Anderson et al. (2001), our results for the magnitudes of assumed constant potentials must be considered average values of the true potentials. The averages are defined by the integrals that appear on the right-hand side of Eq. B2. We have not studied the shape of the Trp potential in this work partly for simplicity, but also because other components of the shape of the proton PMF (Fig. 1 *A*) are missing. This PMF was calculated by molecular dynamics studies that neglected the interaction of an excess proton in the pore with the surrounding membrane and which included only small endcaps of water molecules. It would be necessary to separate any conclusions on the shape of the Trp potential from these missing contributions.

Molecular dynamics studies suggest that the mobility of the gramicidin channel contents decreases as the backbone is made more rigid (Chiu et al., 1991, 1999). Then perhaps Trp indoles help anchor gA to the membrane by making hydrogen bonds with surrounding lipids or interstitial water molecules, decreasing backbone fluctuations and the channel conductance. This mechanism cannot fully explain our conductance data, Fig. 4 *D*, which shows that gA has both increased conductance at low concentrations, as compared with gM, and decreased conductance at high concentrations. However, this effect may occur in combination with the electrostatic mechanism we have considered.

Following the proposal of Phillips et al. (1999) we have also considered whether the voltage-dependent step in the channel, which becomes rate-limiting at the conductance shoulder and which is faster in gM than it is in gA, is water reorientation instead of proton exit. Our conclusion is that water reorientation may play a part in the difference between gA and gM, but probably does not supplant the dominant role of proton exit in gA. Proton exit involves a full elementary charge leaving the pore. Water reorientation involves only a shift in the charge distribution of the overall neutral empty pore. Due to this difference, the energetics of proton exit are more sensitive to the potential difference between gA and gM than the energetics of water reorientation. Changing rates of proton entrance and exit can sufficiently explain a shift by a factor of 100 of the concentration at the onset of the conductance shoulder (Fig. 4) or the similar shift in concentration at which the order of the conductance ratios reverses (Fig. 5). Calculations that consider the energetics of dipoles turning in the perturbing potential due to a Trp → Phe substitution, or consider the energy of the fractional charge associated with bonding defects propagating through the water chain, suggest that perturbed energies probably cannot account for concentration shifts exceeding a factor of four (Busath and Schumaker, unpublished data). Our model results on the time scales of proton exit and water reorientation suggest that direct studies of the water reorientation process are not feasible with gA, but may be possible with gM.

Our sensitivity analysis shows that the peak-to-peak amplitude of the water reorientation barrier calculated by Pomès and Roux (1997; see also Schumaker et al., 2000) using the PM6 water model must be reduced for the single-proton model to successfully fit the data in Fig. 4. Otherwise, water reorientation would be much slower than exit in gM and the dramatic shift in the shoulder seen in Fig. 4 would not occur. A fairly conservative estimate is that the barrier must be decreased by at least 1.5 kcal/mol. Calcu-

lations using the TIP3P model for water give a water reorientation barrier with amplitude reduced by 1.6 kcal/mol, compared with the PM6 calculations (Pomès and Roux, 2002), more consistent with our results. Fig. 8 shows that the quality of the fits continues to improve as the barrier is further decreased in amplitude. The maximum decrease considered is 2.5 kcal/mol ($\Delta\Delta\Phi^{d}_{max} = -2.5$ kcal/mol). We cannot consider lower barriers because the single proton model depends on the lumped-state approximation, which becomes inaccurate if the amplitude of the barrier is decreased still further (Mapes and Schumaker, 2001).

We have interpreted our results to suggest that the amplitude of the water reorientation barrier calculated by Pomès and Roux using the PM6 model must be reduced. However, an alternative interpretation is that the framework model we use is inadequate. The configuration space of the single-proton model does not include states corresponding to an empty pore and an excess proton outside, but close to, the channel entrance. No molecular dynamics simulations are available to guide the inclusion of such states. Therefore, the model implicitly assumes that there is no interaction between pore waters and protons outside the entrance (Schumaker et al., 2001). We cannot exclude the possibility that there is such an interaction, and that it has the effect of catalyzing water reorientation. In this case, the water reorientation barrier in the absence of such a nearby proton may be as high or higher than that depicted by the dots in Fig. 1 *B*. This possibility emphasizes the importance of molecular dynamics simulations of the ion entrance process.

APPENDIX A

Extensions of the proton conduction model

The simplified configuration space for the proton conduction model, Fig. 1 *C*, represents the pore region within which proton and defect transport were simulated by Pomès and Roux (1997). The length of this region is L_P. Let Ψ^s, $s \in \{H, d\}$ denote the component of the potential energy due to an applied transmembrane potential. The case $s = H$ corresponds to the proton-occupied occupied pore and $s = d$ corresponds to the defect-occupied (empty) pore.

$$\Psi^S = \int_{-L_P/2}^{L_P/2} \rho^S(z)V(z)dz \tag{A1}$$

where ρ^S is the charge density of the pore contents and $V(z)$ is the applied electrical potential. V is assumed to be a linear ramp, consistent with the calculations of Jordan (1982) and Roux (1999). For simplicity, the feathering of the potential at the channel entrances found in those calculations is not taken into account. The potential V does not depend on the state s of the pore (Roux, 1997). V extends over the entire length L_T of the channel, including the entrance regions. This gives

$$V = V_I/2 - zE, \quad -L_T/2 < z < L_T/2 \tag{A2}$$

where V_I is the applied electrical potential on side I (see Fig. 1 *C*), z is the spatial coordinate parallel to the pore axis, and $E = V_I/L_T$ is magnitude of the applied electric field. Inserting Eq. A2 into Eq. A1 and integrating, we obtain

$$\Psi^H = e_O V_I/2 - \mu^H E, \tag{A3}$$

$$\Psi^d = -\mu^d E, \tag{A4}$$

where the integral of ρ^d over the pore is zero and the integral of ρ^H over the pore is e_O. The reaction coordinates μ^H and μ^d are axial components of the dipole moments of the pore contents, defined by

$$\mu^S = \int_{-L_P/2}^{L_P/2} \rho^S(z)zdz. \tag{A5}$$

μ^H and μ^d respectively parametrize the top and bottom segments of the simplified configuration space, Fig. 1 *C*, and the state diagram, Fig. 1 *D*. The expressions for Ψ^H and Ψ^d are used to compute electrical potential energy drops around the cycle shown in Fig. 1 *C*. With $\pm\mu^H_A$ and $\pm\mu^d_A$ denoting the extreme values of the proton and defect coordinates, shown on the abscissas of Fig. 1, *A* and *B*, we obtain

$$\Psi^H(-\mu^H_A) - \Psi^H(\mu^H_A) = 2\mu^H_A E, \tag{A6}$$

$$\Psi^H(\mu^H_A) - \Psi^d(-\mu^d_A) = e_O V(L_P/2), \tag{A7}$$

$$\Psi^d(-\mu^d_A) - \Psi^d(\mu^d_A) = 2\mu^d_A E, \tag{A8}$$

$$\Psi^d(\mu^d_A) - \Psi^H(-\mu^H_A) = -e_O V(-L_P/2). \tag{A9}$$

These equations differ from the corresponding equations in Schumaker et al. (2001) only in the right-hand sides of Eqs. A7 and A9. The right-hand side of the equation corresponding to A7 was zero. It is now proportional to $V(L_P/2)$, which is not zero because the linear ramp has been extended to $L_T/2$. The right-hand side of the equation corresponding to A9 was $-e_O V_I$, where $e_O V_I$ is the potential energy of an elementary charge on side I in the presence of the applied potential V_I. The right-hand side of Eq. A9 is proportional to $V(-L_P/2)$. This is less than V_I, reflecting the electrical potential drop between the bulk solution and $z = -L_P/2$. Adding Eqs. A6–A9 together and dividing by E gives

$$2\mu^H_A + 2\mu^d_A = e_O L_P \tag{A10}$$

The extent of the reaction coordinates in the simulations of Pomès and Roux is identified with the pore length L_P, which is less than the total length L_T.

The pairs of dashed lines in Fig. 1 *C* indicate two continuous families of transition possible between the proton and defect segments of the configuration space. Physically, these model the fact that when an excess proton leaves the channel, the pore waters may be in a range of states. The lumped state approximation (Schumaker et al., 2000, 2001) assumes that the two ranges of states are localized in boundary regions near the ends of the defect segment (see Fig. 1 *B*). Transitions between the proton and defect segments are then simplified by lumping the boundary region between μ^d_C and μ^d_A into a single point, the boundary state b_I, and by lumping the boundary region between $-\mu^d_A$ and $-\mu^d_C$ into the state by b_{II}. The boundary states must be assigned effective coordinates to model their response to an applied electric field. Optimal coordinates are average values of μ^d in the boundary regions, weighted by the Boltzmann factor $\exp(-\beta\Phi^d)$ (Mapes and Schumaker, 2001). Denoting these averages $\pm\mu_B$, we define fractional electrical distances in a manner similar to that given by Schumaker et al. (2001), but with L_T replacing L_P. In particular, the

electrical distance between the boundary regions and the endpoints of the defect segment is given by

$$f_A^d = (\mu_A^d - \mu_B^d)/(e_O L_T), \quad \text{(A11)}$$

This corresponds to the electrical distance associated with proton exit in Schumaker et al. (2001). To model the total electrical distance associated with the channel entrance regions, we add to f_A^d an electrical distance corresponding to the physical displacement of an elementary charge passing through the entrance regions $|L_P/2| < |z| < |L_T/2|$. The total electrical distance corresponding to proton entrance or exit is now f_E, where

$$f_E = f_A^d + (1/2)e_O(L_T - L_P)/(e_O L_T). \quad \text{(A12)}$$

The electrical distance f_E is decomposed according to Eq. 1, and f_N and f_X are used in modified expressions for the proton entrance and exit transition probabilities of the random walk whose limit gives the proton conduction model (Schumaker et al., 2001; compare with Eqs. 49–51):

$$\alpha_I^Z = \Delta t(t^{aZ})^{-1}a^{-1}C_-^{-1}\exp\beta(\zeta^Z + f_N^Z\Psi_I), \quad \text{(A13)}$$

$$\alpha_{II}^Z = \Delta t(t^{aZ})^{-1}a^{-1}C_-^{-1}\exp\beta(\zeta^Z - f_N^Z\Psi_I), \quad \text{(A14)}$$

$$\beta_I^Z = \Delta t(t^{aZ})^{-1}n\exp(-\beta f_X^Z\Psi_I), \quad \text{(A15)}$$

$$\beta_{II}^Z = \Delta t(t^{aZ})^{-1}n\exp(\beta f_X^Z\Psi_I). \quad \text{(A16)}$$

The superscript $Z \in \{A, B, M\}$. For gA, $f_N^A = 0$ and $f_X^A = f_E$. The integer n gives the number of states in the proton and defect segments of the random walk, and $\Delta t = \Delta\tau/n^2$ is the random walk time step, with $\Delta\tau$ independent of n. The limit $n \to \infty$ gives the proton conductance model. The weight a of the boundary states is proportional to the integral of $\exp(-\beta\Phi^d)$ over the boundary regions (Eq. 65 in Schumaker et al., 2001). C_- is the unit concentration. Fits of the gA model to the data in Fig. 4 *A* optimize the values of t^{aA} and ζ^A, which are used to control the entrance and exit rates. f_N^Z, $Z \in \{B, M\}$ is one free parameter in the fits of the gB and gM models to their current data. A second free parameter determined the values of t^{aZ} and ζ^Z used for gB and gM as described in Appendix B (see Eqs. B4 and B5).

APPENDIX B

Consequences of statistical mechanics

In this Appendix we apply statistical mechanics to the pore of gramicidin assuming that it is occupied by at most a single proton at one time. At thermodynamic equilibrium, the probability that an excess proton will occupy the pore of g*Z*, $Z \in \{A, B, M\}$ is given by (Schumaker et al., 2001)

$$Q^{HZ} = \frac{\int e^{-\beta W^{HZ}}d\mu^H}{\int e^{-\beta W^{HZ}}d\mu^H + (C_H/C_I)e^{-\beta\Psi_I}\int e^{-\beta W^{dZ}}d\mu^d}, \quad \text{(B1)}$$

where integration takes place over the intervals $-\mu_A^H \le \mu^H \le \mu_A^H$ and $-\mu_A^d \le \mu^d \le \mu_A^d$. The total energy of an ion at reaction coordinate μ^H is $W^{HZ}(\mu^H) = \Phi^{HZ}(\mu^H) + \Psi^{HZ}(\mu^H)$, where Φ^{HZ} is the intrinsic and Ψ^{HZ} the applied potential energy. Similarly, the total energy of an empty pore with a defect at coordinate μ^d is $W^{dZ}(\mu^d) = \Phi^{dZ}(\mu^d) + \Psi^{dZ}(\mu^d)$. C_I is the proton concentration in the bulk solution on side I of the channel, C_H is a constant with units of concentration, and $\beta = 1/(k_B T)$. The probability that the channel is empty is $Q^{dZ} = 1 - Q^{HZ}$. It follows that

$$Q^{HZ}/Q^{dZ} = (C_I/C_H)e^{\beta\Psi_I}\left(\int e^{-\beta W^{HZ}}d\mu^H \Big/ \int e^{-\beta W^{dZ}}d\mu^d\right). \quad \text{(B2)}$$

These formulas hold for both the original single proton model (Schumaker et al., 2001) and the extended model considered here.

Scaling of entrance and exit rates

As described in Materials and Methods, we assume that the difference in occupied state intrinsic potential energy between g*Z*, $Z \in \{B, M\}$, and gA is a constant independent of μ^H (or equivalently, the spatial coordinate z). This difference is denoted $\delta\Phi^Z$ and is given by Eq. 2. Using this and Eq. 3, Eq. B2 gives

$$(Q^{HZ}/Q^{dZ}) = (Q^{HA}/Q^{dA})\exp(-\beta\delta\Phi^Z). \quad \text{(B3)}$$

$\delta\Phi^Z$ is decomposed according to Eq. 4. Entrance and exit rates for g*Z* are obtained by scaling t^{aZ} and ζ^Z so that

$$\alpha_R^Z = \alpha_R^A\exp(-\beta\delta\Phi^{NZ}), \quad \text{(B4)}$$

$$\beta_R^Z = \beta_R^A\exp(\beta\delta\Phi^{XZ}), \quad \text{(B5)}$$

where $R \in \{I, II\}$. For example, since both $\delta\Phi^{NM} > 0$ and $\delta\Phi^{XM} > 0$, the increased energy of excess protons in the pore of gM is reflected in both a decreased entrance rate and an increased exit rate relative to gA.

Pore volume and C_H

At sufficiently low free proton concentrations in bulk, $Q^{dZ} \approx 1$ and Eq. B2 is well-approximated by

$$Q^{HZ} = (C_I/C_H)e^{\beta\Psi_I}\left(\int e^{-\beta W^{HZ}}d\mu^H \Big/ \int e^{-\beta W^{dZ}}d\mu^d\right). \quad \text{(B6)}$$

We now drop the superscript *Z* specifying the analog. Consider this formula at a symmetrical equilibrium: $\Psi_I = 0$ and $C_I = C_{II}$. Further suppose that the intrinsic proton and water reorientation PMFs are zero, then $W^H = W^d = 0$. Eq. B6 becomes

$$Q^H = (C_I/C_H)(\mu_A^H/\mu_A^d) \quad \text{(B7)}$$

Since $W^H = 0$, the probability that the pore is occupied is equal to the bulk concentration of excess protons times an effective pore volume:

$$Q^H = C_I V_{pore}. \quad \text{(B8)}$$

Assuming that the pore of gramicidin holds 10 water molecules, V_{pore} is the volume that would be occupied by 10 water molecules in the bulk solution. Combining B7 and B8 gives a formula for C_H:

$$C_H^{-1} = V_{pore}(\mu_A^d/\mu_A^H). \quad \text{(B9)}$$

Schumaker et al. (2001) introduce another constant, $C_0 = C_H(\mu_C^d/\mu_A^H)$. Equation B9 then implies $C_0^{-1} = (\mu_A^d/\mu_C^d)V_{pore}$. In the reference cited above, the right-hand sides of Eqs. 35 and 36 and the left-hand side of Eq. 38 should be multiplied by the factor μ_A^H/μ_C^d.

Single-proton model dissociation constant

The dissociation constant is the concentration at which the probability of proton occupation is 50%. The association constant K_Z, for $Z \in \{A, B, M\}$, is the inverse of this concentration. From Eq. B2

$$K_Z C_\bullet = (C_\bullet/C_H) e^{\beta\Psi_I} \left(\int e^{-\beta W^{HZ}} d\mu^H \Big/ \int e^{-\beta W^{dZ}} d\mu^d \right), \tag{B10}$$

where $C_\bullet$ is the unit concentration. At a symmetrical equilibrium, $C_I = C_{II}$ and $\Psi_I = 0$, we have

$$W^{HZ}(\mu^H) = \Phi^{HZ}(\mu^H) = \Phi^{HZ}_A + \Delta\Phi^H(\mu^H), \tag{B11}$$

$$W^{dZ}(\mu^d) = \Phi^{dZ}(\mu^d) = \Phi^d_C + \Delta\Phi^d(\mu^d), \tag{B12}$$

where the intrinsic potentials Φ^{HZ} and Φ^{dZ} are decomposed into relative potentials $\Delta\Phi^H$ and $\Delta\Phi^d$ and absolute energies $\Phi^{HZ}_A = \Phi^{HZ}(\mu^H_A)$ and $\Phi^d_C = \Phi^{dZ}(\mu^d_C)$. According to our model of intrinsic potentials, Eqs. 2 and 3, only the absolute component of the proton potential depends on the analog Z. We further introduce the parameter ζ^Z defined by

$$\zeta^Z = \Phi^d_C - \Phi^{HZ}_A - k_B T \ln(C_O/C_\bullet) \tag{B13}$$

(Schumaker et al., 2001) and note the relationship between C_H and C_O defined below Eq. B9. Combining these expressions, we obtain

$$K_Z C_\bullet = (\mu^d_C/\mu^H_A) e^{\zeta^Z} \left(\int e^{-\beta\Delta\Phi^H} d\mu^H \Big/ \int e^{-\beta\Delta\Phi^d} d\mu^d \right). \tag{B14}$$

This equation is used to evaluate dissociation constants from model fits to the data. Dissociation constants calculated this way are $K_A^{-1} = 11$ mM, $K_B^{-1} = 32$ mM, and $K_M^{-1} = 2.2$ M. The first two values are in good agreement with the simple estimates made directly from the data below Eq. 7. This supports our use of the concentration at which the current ratios reverse as an empirical estimate of the dissociation constant. The last estimate is higher than the estimate $K_M^{-1} \approx 1$ M made from the data. This discrepancy reflects the fact that the model curve ratios shown in Fig. 5 *C* (*solid curves*) reverse at a value that is somewhat greater than suggested by the data.

Excess proton energy in the pore relative to energy in the bulk

We calculate the energy levels for protons in the pore of gA, gB, and gM relative to the bulk in Fig. 9 by considering the extent to which protons are concentrated in the pore of each analog in the limit of low excess proton concentrations in the bulk. It is important to take this limit so that the single proton restriction has no influence on the proton concentrations in the pore. Consider Eq. B6 at a symmetrical equilibrium, $C_I = C_{II} = 0$ and $\Psi_I = 0$, so that Eqs. B11 and B12 hold. Then

$$Q^{HZ} = (C_I/C_H) e^{\beta(\Phi^d_C - \Phi^{HZ}_A)} \left(\int e^{-\beta\Delta\Phi^H} d\mu^H \Big/ \int e^{-\beta\Delta\Phi^d} d\mu^d \right). \tag{B15}$$

Substituting the relationship between C_H and C_O from below Eq. B9, and the definition of ζ^Z from Eq. B13, we have the computational form for Q^{HZ} in the limit of low bulk proton concentration:

$$Q^{HZ} = C_I K_Z. \tag{B16}$$

This is the probability of finding an excess proton among 10 water molecules in the channel. Compare this with the probability of finding an excess proton among 10 water molecules in bulk; this latter quantity is given by $10C_I/C_W$, where $C_W = 55$ M is the concentration of water in bulk. We then define the absolute energy Φ^{HZ}_A of an excess proton in the pore of the analog channel gZ by the prescription that the average value of the Boltzmann factor is equal to the extent to which protons are concentrated in the pore:

$$\int e^{-\beta\Phi^{HZ}} d\mu^H/(2\mu^H_A) = Q^{HZ}/(10C_I/C_W) \tag{B17}$$

The Φ^{HZ}_A are used to define the energy levels shown in Fig. 9.

APPENDIX C

Proton mean time before exit

Boundary value problem

Let $\bar{t}(\mu)$ be the mean first passage time before a proton, starting at reaction coordinate $\mu \in [-\mu^H_A, \mu^H_A]$, first exits the pore. Mapes and Schumaker (2001) give a derivation of a differential equation for $\bar{t}$ based on the diffusion limit of a random walk. Transition probabilities in the pore interior are described by Schumaker et al. (2001), and entrance and exit transition probabilities are given by Eqs. A13–A16. Following the method of Mapes and Schumaker, boundary conditions on $\bar{t}$ may also be obtained, yielding the boundary value problem:

$$-1 = \mathcal{D}[\bar{t}''(\mu) - \beta W'(\mu)\bar{t}'(\mu)]. \tag{C1}$$

where

$$\mathcal{D}\bar{t}'(-\mu_A) = (t^a)^{-1}\mathcal{L} \exp(-\beta f_X \Psi_I)\bar{t}(-\mu_A) \tag{C2}$$

$$\mathcal{D}\bar{t}'(\mu_A) = -(t^a)^{-1}\mathcal{L} \exp(\beta f_X \Psi_I)\bar{t}(\mu_A). \tag{C3}$$

Solution

We have solved Eq. C1 with boundary conditions, Eqs. C2 and C3, to obtain the exact solution for $\bar{t}(\mu)$ using variation of parameters, similar to the calculation shown by Mapes and Schumaker (2001). The calculation is somewhat lengthy and the result fairly complicated. To check it, we also solved the boundary value problem numerically using the method of shooting (Press et al., 1992; Ruskeepää, 1999). The variations of $\bar{t}$ with μ given by the numerical and exact solutions were very similar. These results hold for several cases involving gA, gB, and gM, and both with and without applied potential and confirm the exact solution. Values of the proton reaction coordinate μ and an effective value z for the coordinate of the proton in the channel are proportional to each other (Schumaker et al., 2000). The relationship is defined by requiring that $\mu = -\mu^H_A$ correspond at $z = -L_P/2$ and that $\mu = \mu^H_A$ correspond to $z = L_P/2$. Using the relationship of z to μ, Fig. 7 presents examples of the exact solution for $\bar{t}$ as a function of z.

When the applied potential is zero, differences in the solutions for $\bar{t}$ are due only to the boundary conditions C2 and C3. For $\Psi_I = 0$, these boundary conditions differ only in the values of t^a, and these values appears only in the ratios $\bar{t}(\mu_A)/t^a$ and $\bar{t}(-\mu_A)/t^a$. The values of t^a for gB and gM are determined by the requirement that Eqs. B4 and B5 are satisfied. For gA,

gB, and gM, the values of t^a are 21.9, 8.52, and 0.335 ns, respectively. Given $\bar{\tau}$ for gA, the mean times to exit for gB and gM are obtained by scaling $\bar{\tau}(-\mu_A) = \bar{\tau}(\mu_A)$ in proportion to t^a. When the applied potential is different from zero, potential-dependent factors now enter into Eqs. C1 through C3, and the shapes of $\bar{\tau}(z)$ are not identical for all of the analogs.

The authors thank Sam Cukierman and Régis Pomès for helpful discussions. M.F.S. thanks Arnd Roth for providing an updated version of his ActivityCoefficients package for Mathematica.

This work was supported by National Science Foundation Grant 9630475 (to M.F.S.) and National Institutes of Health Grant R01 AI23007 (to D.B.).

REFERENCES

Andersen, O. S. 1983. Ion movement through gramicidin A channels. Interfacial polarization effects on single-channel current measurements. *Biophys. J.* 41:135–146.

Andersen, O. S. 1999. Graphic representation of the results of kinetic analyses. *J. Gen. Physiol.* 114:589–590.

Andersen, O. S., D. V. Greathouse, L. L. Providence, M. D. Becker, and R. E. Koeppe II. 1998. Importance of tryptophan dipoles for protein function: 5-fluorination of tryptophans in gramicidin A channels. *J. Am. Chem. Soc.* 120:5142–5146.

Anderson, D., R. B. Shirts, T. A. Cross, and D. D. Busath. 2001. Noncontact dipole effects on channel permeation. V. Computed potentials for fluorinated gramicidin. *Biophys. J.* 81:1255–1264.

Arsenyev, A. S., A. L. Lomize, I. L. Barsukov, and V. F. Bystrov. 1990. Gramicidin A transmembrane channel. Three-dimensional structural rearrangement based on NMR spectroscopy and energy refinement. *Biol. Mem.* 3:1723–1778.

Becker, M. D., D. V. Greathouse, R. E. Koeppe II, and O. S. Andersen. 1991. Amino acid sequence modulation of gramicidin channel function: effects of tryptophan-to-phenylalanine substitutions on the single-channel conductance and duration. *Biochemistry.* 30:8830–8839.

Becker, M. D., R. E. Koeppe II, and O. S. Andersen. 1992. Amino acid substitutions and ion channel function: model-dependent conclusions. *Biophys. J.* 62:25–27.

Busath, D. D. 1993. The use of physical methods in determining gramicidin channel structure and function. *Annu. Rev. Physiol.* 55:473–501.

Busath, D. D., C. D. Thulin, R. W. Hendershot, L. R. Phillips, P. Maughan, C. D. Cole, N. C. Bingham, S. Morrison, L. C. Baird, R. J. Hendershot, M. Cotten, and T. A. Cross. 1998. Non-contact dipole effects on channel permeation. I. Experiments with (5F-indole)Trp-13 gramicidin A channels. *Biophys. J.* 75:2830–2844.

Chiu, S.-W., E. Jakobsson, S. Subramanian, and J. Andrew McCammon. 1991. Time-correlation analysis of simulated water motion in flexible and rigid gramicidin channels. *Biophys. J.* 60:273–285.

Chiu, S.-W., S. Subramanian, and E. Jakobsson. 1999. Simulation study of a gramicidin/lipid bilayer system in excess water and lipid. II. Rates and mechanisms of water transport. *Biophys. J.* 76:1939–1950.

Corry, B., S. Kuyucak, and S. H. Chung. 2000. Tests of continuum theories as models of ion channels. II. Poisson-Nernst-Planck theory versus Brownian dynamics. *Biophys. J.* 78:2364–2381.

Cotten, M., R. Fu, and T. A. Cross. 1999a. Solid-state NMR and hydrogen-deuterium exchange in a bilayer-solubilized peptide: structural and mechanistic implications. *Biophys. J.* 76:1179–1189.

Cotten, M., C. Tian, D. D. Busath, R. B. Shirts, and T. A. Cross. 1999b. Modulating dipoles for structure-function correlations in the gramicidin A channel. *Biochemistry.* 38:9185–9197.

Cukierman, S. 2000. Proton mobilities in water and in different stereoisomers of covalently linked gramicidin A channels. *Biophys. J.* 78: 1825–1834.

DeCoursey, T. E., and V. V. Cherny. 1999. An electrophysiological comparison of voltage-gated proton channels, other ion channels, and other proton channels. *Israel J. Chem.* 39:409–418.

De Godoy, C. M. G., and S. Cukierman. 2001. Modulation of proton transfer in the water wire of dioxolane-linked gramicidin channels by lipid membranes. *Biophys. J.* 81:1430–1438.

Dorigo, A. E., D. G. Anderson, and D. D. Busath. 1999. Noncontact dipole effects on channel permeation. II. Trp conformations and dipole potentials in gramicidin A. *Biophys. J.* 76:1897–1908.

Duca, K. A., and P. C. Jordan. 1998. Comparison of selectively polarizable force fields for ion-water-peptide interactions: ion translocation in a gramicidin-like channel. *J. Phys. Chem. B.* 102:9127–9138.

Eisenman, G., B. Enos, J. Hagglund, and J. Sandblom. 1980. Gramicidin as an example of a single-filing ionic channel. *Ann. NY. Acad. Sci.* 339: 8–20.

Heitz, F., G. Spach, and Y. Trudelle. 1982. Single channels of 9,11,13,15-destryptophyl-phenylalanyl-gramicidin A. *Biophys. J.* 40:87–89.

Hladky, S. B. 1999. Can we use rate constants and state models to describe ion transport through gramicidin channels? *Novartis Found. Symp.* 225: 93–107.

Hu, W., and T. A. Cross. 1995. Tryptophan hydrogen bonding and electrical dipole moments: functional roles in the gramicidin channel and implications for membrane proteins. *Biochemistry.* 34:14147–14155.

Hu, W., N. D. Lazo, and T. A. Cross. 1995. Tryptophan dynamics and structural refinement in a lipid bilayer environment: solid state NMR of the gramicidin channel. *Biochemistry.* 34:14138–14146.

Hu, W., K.-C. Lee, and T. A. Cross. 1993. Tryptophans in membrane proteins: indole ring orientations in the gramicidin channel. *Biochemistry.* 32:7035–7047.

Jaikaran, D. C. J., and G. A. Woolley. 1995. Characterization of thermal isomerization at the single molecule level. *J. Phys. Chem.* 99: 13352–13355.

Jordan, P. C. 1982. Electrostatic modeling of ion pores. Energy barriers and electric field profiles. *Biophys. J.* 39:157–164.

Ketchem, R. R., B. Roux, and T. A. Cross. 1997. High-resolution polypeptide structure in a lamellar phase lipid environment from solid state NMR derived orientational constraints. *Structure.* 5:1655–1669.

Koeppe, II, R. E., and L. B. Weiss. 1981. Resolution of linear gramicidins by preparative reversed-phase high-performance liquid chromatography. *J. Chromatagr.* 208:414–418.

Mapes, E., and M. F. Schumaker. 2001. Mean first passage times across a potential barrier in the lumped state approximation. *J. Chem. Phys.* 114:76–83.

Markham, J. C., J. A. Gowen, T. A. Cross, and D. D. Busath. 2001. Comparison of gramicidin A and gramicidin M channel conductance dispersities. *Biochim. Biophys. Acta.* 1513:185–192.

Miller, C. 1999. Ionic hopping defended. *J. Gen. Physiol.* 113:783–787.

Moy, G., B. Corry, S. Kuyucak, and S. H. Chung. 2000. Tests of continuum theories as models of ion channels. I. Poisson-Boltzmann theory versus Brownian dynamics. *Biophys. J.* 78:2349–2363.

Neher, E., J. Sandblom, and G. Eisenman. 1978. Ionic selectivity, saturation, and block in gramicidin A channels. II. Saturation behavior of single channel conductances and evidence for the existence of multiple binding sites in the channel. *J. Membr. Biol.* 40:97–116.

Phillips, L. R., C. D. Cole, R. J. Hendershot, M. Cotten, T. A. Cross, and D. D. Busath. 1999. Noncontact dipole effects on channel permeation. III. Anomalous proton conductance effects in gramicidin. *Biophys. J.* 77:2492–2501.

Pomès, R. 1999. Theoretical studies of the Grotthus mechanism in biological proton wires. *Israel J. Chem.* 39:387–395.

Pomès, R., and B. Roux. 1996. Structure and dynamics of a proton wire: a theoretical study of H^+ translocation along the single-file water chain in the gramicidin A channel. *Biophys. J.* 71:19–39.

Pomès, R., and B. Roux. 1997. Free energy profiles governing H^+ conductance in proton wires. *Biophys. J.* 72:246*a* (Abstr.).

Pomès, R., and B. Roux. 1998. Free energy profiles for H^+ conduction along hydrogen-bonded chains of water molecules. *Biophys. J.* 75: 33–40.

Pomès R., and B. Roux. 2002. Molecular mechanism of H^+ conduction in the single-file water chain of the gramicidin channel. *Biophys. J.* 82: 2304–2316.

Press, W. H., S. A. Teukolsky, W. T. Vetterling, and B. P. Flannery. 1992. Numerical Recipes in Fortran. Cambridge University Press, New York. 653–655; 749–751.

Quigley, E. P., D. S. Crumrine, and S. Cukierman. 2000. Gating and permeation in ion channels formed by gramicidin A and its dioxolane-linked dimer in Na^+ and Cs^+ solutions. *J. Membr. Biol.* 174:207–212.

Rokitskaya, T. I., E. A. Kotova, and Y. N. Antonenko. 2002. Membrane dipole potential modulates proton conductance through gramicidin channel: movement of negative ionic defects inside the channel. *Biophys. J.* 82:865–873.

Roux, B. 1997. Influence of the membrane potential on the free energy of an intrinsic protein. *Biophys. J.* 73:2980–2989.

Roux, B. 1999. Statistical mechanical equilibrium theory of selective ion channels. *Biophys. J.* 77:139–153.

Ruskeepää, H. 1999. Mathematica Navigator. Academic Press, New York. 690–691.

Schumaker, M. F., R. Pomès, and B. Roux. 2000. A combined molecular dynamics and diffusion model of single proton conduction through gramicidin. *Biophys. J.* 79:2840–2857.

Schumaker, M. F., R. Pomès, and B. Roux. 2001. A framework model for single proton conductance through gramicidin. *Biophys. J.* 80:12–30.

Thompson, N., G. Thompson, C. D. Cole, M. Cotten, T. A. Cross, and D. D. Busath. 2001. Non-contact dipole effects on channel permeation. IV. Kinetic model of $5F\text{-}Trp_{13}$ gramicidin A currents. *Biophys. J.* 81: 1245–1254.

Urry, D. W., M. C. Goodall, J. D. Glickson, and D. F. Mayers. 1971. The gramicidin A transmembrane channel: characteristics of head-to-head dimerized $\pi_{(L,D)}$ helices. *Proc. Natl. Acad. Sci.* U.S.A. 68: 1907–1911.

Wallace, B. A. 1990. Gramicidin channels and pores. *Annu. Rev. Biophys. Biophys. Chem.* 19:127–157.

Woolf, T. B., and B. Roux. 1997. The binding site of sodium in the gramicidin A channel: comparison of molecular dynamics with solid-state NMR data. *Biophys. J.* 72:1930–1945.

Woolley, G. A., and B. A. Wallace. 1992. Model ion channels: gramicidin and alamethicin. *J. Membr. Biol.* 129:109–136.